Development of a Turbulent Liquid Spray Atomization Model for Diesel Engine Simulations

Final Technical Report

US Department of Energy Award DE-EE0007333

Project Period: January 2016 – Sept 2019

PI:
Caroline L. Genzale
Associate Professor
G.W. Woodruff School of Mechanical Engineering
Georgia Institute of Technology

Partner Organization:
Argonne National Laboratory

Report Submitted: June 3, 2021

Executive Summary

This project addresses the systematic lack of predictive capabilities by spray models within engine CFD codes. We develop a new modeling approach to predict the breakup of diesel sprays based on recent literature showing that liquid turbulence plays a fundamental role in spray atomization. A new body of quantitative validation data is also developed as a critical element of the project, leveraging the joint capabilities of Georgia Tech's high-pressure continuous-flow spray chamber and Argonne National Lab's near-nozzle x-ray diagnostics at the Advanced Photon Source. This project contributes spatially-resolved measurements of drop size distribution within well-characterized diesel injectors, Spray A and D, from the Engine Combustion Network (ECN) to the engine combustion community for the first time. Utilizing this new body of measurements, we validate and demonstrate a new spray model for diesel sprays, termed the KH-Faeth model, that predicts global and *local* spray characteristic more accurately than the widely adopted and employed KH model. Predicted drop size distributions are seen to predict measured drops sizes both quantitatively and predictively, with accurate response in droplet size distributions over a wide range of ambient density, injection pressure, and injector nozzle size (Spray A and D) without model tuning. The KH-Faeth model can reduce error in the predicted centerline droplet size profile by up to 80% for ECN Spray D simulations when compared to use of the widely employed KH model

Table of Contents

1 Project Summary

This project addresses the systematic lack of predictive capabilities by spray models within engine CFD codes. We develop a new modeling approach to predict the breakup of diesel sprays based on recent literature showing that liquid turbulence plays a fundamental role in spray atomization. A new body of validation data is also developed as a critical element of the project leveraging the joint capabilities of Georgia Tech's high-pressure continuous-flow spray chamber and Argonne National Lab's near-nozzle x-ray diagnostics at the Advanced Photon Source. Joint measurements at the two institutions yield measurements of drop size distribution within diesel sprays over a wide range of engine-relevant conditions.

2 Project Objectives and Approach

2.1 Overall Objective

- Develop a new spray atomization model for engine CFD codes with improved prediction accuracy for local spray morphology and global spray characteristics over a wide range of engine operating conditions, including conditions relevant for advanced combustion engines.
- Improve understanding of fundamental physics governing atomization in diesel fuel sprays, especially for advanced combustion regimes.
- Develop and apply a new diagnostic (SAMR) to measure spatially-resolved distributions of Sauter Mean Diameter (SMD) over a wide range of engine-relevant operating conditions.

2.2 Overall Approach

Two new droplet measurement diagnostics are developed to address the existing spray measurement gaps in real-world fuel injection sprays at engine-relevant operating conditions. These new measurements then provide the necessary physical insight to formulate and validate a new, more predictive, spray atomization model for engine CFD codes. First, a new x-ray scattering diagnostic under recent development at Argonne National Lab, Ultra Small Angle X-ray Scattering (USAXS), is applied to diesel sprays to quantify droplet sizes within optically thick regions near the injector nozzle and along the spray centerline. Second, a new 2-D measurement technique is developed to quantify the spatially resolved atomization of diesel sprays. The new diagnostic, termed the Scattering-Absorption Measurement Ratio (SAMR), results from coupling two measurements performed at two institutions: 1) 2-D measurements of optical thickness via liquid-scattering extinction, performed at Georgia Tech; and 2) 2-D measurements of liquid volume fraction via x-ray radiography, performed at Argonne National Lab. A ratio of the two measurements yields the spatially resolved Sauter Mean Diameter (SMD). Diesel spray experiments are replicated at the two institutions using shared Engine Combustion Network (ECN) Spray D and Spray A injectors. Several existing spray atomization models are then benchmarked against this data to identify model formulation inaccuracies, leading to the formulation of a new modeling approach that incorporates fundamental understanding gleaned from the USAXS and SAMR measurement campaigns. The measurement campaign and new spray atomization modeling approach are formulated based on the hypothesis that liquid turbulence plays an important contributing role in spray breakup, especially under low ambient density conditions of relevance for advanced combustion engines.

3 Key Accomplishments

- Demonstrated a new spray atomization CFD model for diesel sprays, termed the KH-Faeth model, that predicts global and *local* spray characteristic more accurately than the widely adopted and employed KH model. Predicted drop size distributions are seen to predict measured drops sizes both quantitatively and predictively, with accurate response in droplet size distributions over a wide range of ambient density, injection pressure, and injector nozzle size (Spray A and D) without model tuning.
- Showed that the KH-Faeth model employed into engine CFD simulations can reduce error in the predicted centerline droplet Sauter Mean Diameter (SMD) by up to 80% for ECN Spray D simulations when compared to use of the widely employed KH model.
- Measured the near-nozzle centerline SMD distribution of ECN Spray D for the first time using a new x-ray scattering diagnostic (USAXS) developed at Argonne National Lab.
- Measured the 2D SMD distribution produced by ECN Spray A and Spray D for the first time using a new diagnostic developed as part of this project, termed the Scattering-Absorption Measurement Ratio (SAMR).
- Created a large database of spatially-resolved drop size measurements for future spray model development and validation from two well-characterized research injectors (Spray A and D). The database includes experiments from a wide range of ambient densities (1.2 – 22.8 kg/m3) and injection pressures (500 and 1500 bar) under non-vaporizing conditions.

4 Approach

4.1 Generate Validation Data (SOPO Task 1)

4.1.1 GA Tech Experimental Facility: High-Pressure and Temperature (HiPT) Spray Combustion Chamber

This work was performed in a nominally quiescent spray chamber without the complications of in-cylinder flows, thus minimizing confounding flow effects on spray atomization. This facility, shown in Figure 1, is capable of creating a high-pressure (3 bar to 100 bar) and high-temperature (293 K to 950 K) environment in which to optically probe a fuel injection event. The vessel is a two-part design with an outer chamber to hold pressure while the inner chamber is insulated to contain the high temperature gases. High pressure air is fed through the bottom of the vessel and passes through two 15-kW electrical heaters to raise the temperature of the incoming air. Then, the air enters the insulated inner chamber through a diffuser designed to promote temperature uniformity within the test section. Directly beneath the diffuser lies an additional 5-kW heater to further enable temperature uniformity. The injector is mounted in a cooling jacket such that with vessel heating, the injector body temperature can be controlled down to 80°C. Four sets of quartz windows (one set is not visible due to the cut-away and is located along the spray axis) surround the spray providing 100 mm of optical access.

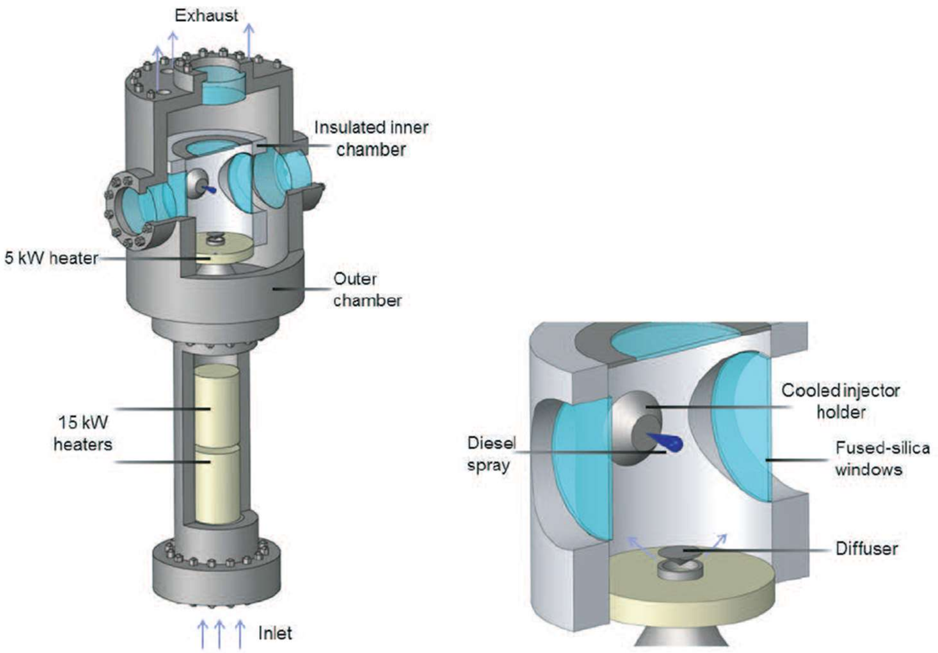

Figure 1: Cut-away schematic of high-pressure and temperature (HiPT) spray chamber at Georgia Tech.

4.1.2 GA Tech Experiments: Diffuse Back-Illumination (DBI) Measurements of Spray Optical Thickness Distribution

Measurements of spray optical thickness were conducted using Diffuse Back-Illumination (DBI) imaging. The DBI imaging setup was based on recommendations by the Engine Combustion Network (ECN), as documented in Westlye et al. [1]. The DBI setup creates a diffuse light source to illuminate the spray field. An extended and spatially uniform light source with constant radiance is desired to maximize the light throughput [1]. A Photron SA-X2 camera with a CMOS image sensor was used to measure the intensity of incident and attenuated light.

The Beer-Lambert law is used to relate the attenuation of light through a material. Light attenuation includes absorption and scattering. The optical thickness (τ) can be calculated using the Beer-Lambert law, which relates the incident light intensity (I_o) to the attenuated light intensity (I):

$$\frac{I}{I_o} = e^{-\tau} \tag{1}$$

$$\tau = -\ln\left(\frac{I}{I_o}\right) \tag{2}$$

A high-power, pulsed LightSpeed Technologies LED served as the light source for these DBI experiments. The LED illuminates the chamber before the fuel injection begins enabling a 2D measurement of I_o. After the start of injection, the high-speed camera records the attenuated light, I, after passing through the spray. At the visible wavelengths used for this work, the light extinction is dominated by light scattering from the surface of fuel droplets.

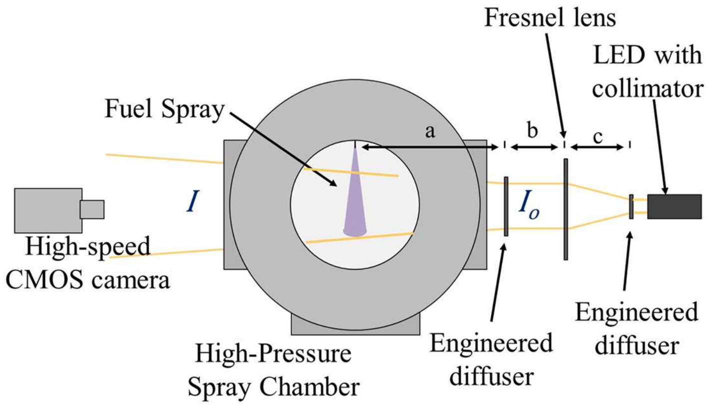

Figure 2: Schematic of the DBI measurement setup at Georgia Tech.

Table 1: Optical setup dimensions for each phase of the project. Dimension variables illustrated in Figure 2.

	Phase I	**Phase II**	**Phase III**
a	250 mm	250 mm	258 mm
b	140 mm	140 mm	640 mm
c	152 mm	152 mm	180 mm

Figure 2 shows the schematic of the experimental setup utilized for the DBI experiments, with optical setup dimensions referenced in Table 1. This setup follows the recommendations of Westlye and co-workers for DBI used in diesel-relevant sprays employed in high-pressure high-temperature spray chambers, In Phase III, the DBI setup was modified from the DBI setup recommended by Westlye to create an optimized DBI setup for the SAMR technique. Table 2 shows the camera and light source settings for each phase of the work.

Figure 3 shows and example measured optical thickness map from the DBI experiments for Spray D $\rho_{amb} = 1.2$ kg/m^3 $P_{inj} = 50$ MPa. The DBI data is time averaged to attain the steady portion of the spray and ensemble averaged to reduce errors associated with shot-to-shot variation.

Table 2: Camera and light source settings for all phases of the work.

	Camera Lens	Camera Frame Rate	LED pulse rate	Pulse width	Half Collection Angle	Projected Pixel Size
Phase I	50mm f/1.2	72,000 fps	36,000 fps	90 ns	4.85°	77.7 µm/pixel
Phase II	50mm f/2.8	72,000 fps	36,000 fps	52 ns	4.16°	94.6 µm/pixel
Phase III	85 mm f/1.8	72,000 fps	72,000 fps	78 ns	3.67°	66.0 µm/pixel

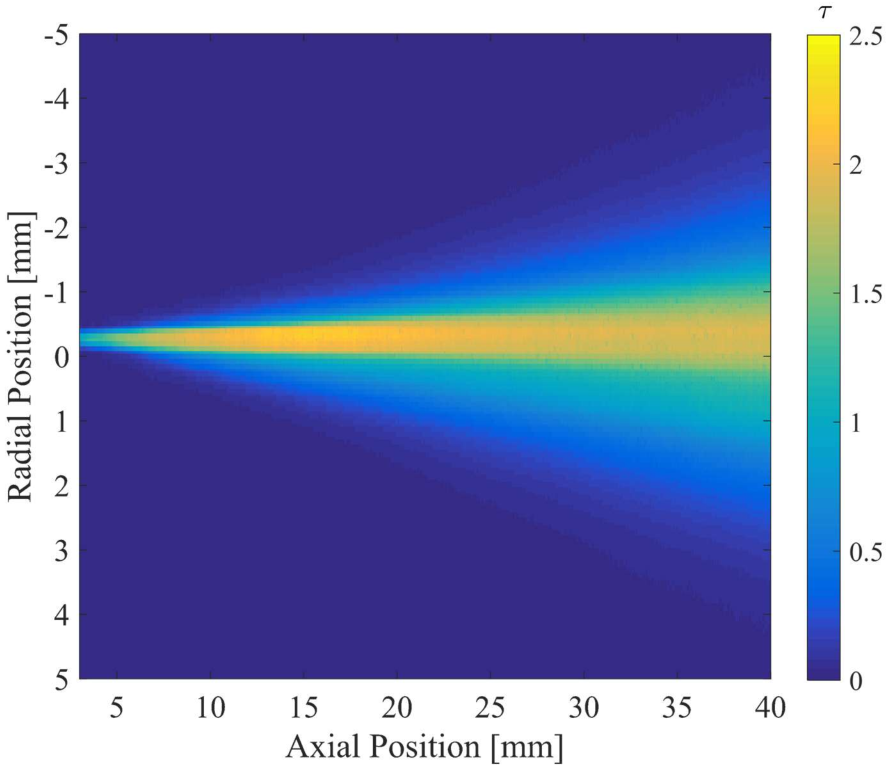

Figure 3: Measured optical thickness map for Spray D. Conditions: ρ_{amb} = 1.2 kg/m^3, P_{inj} = 50 MPa, 120° injector orientation.

4.1.3 *Argonne Experiments: X-Ray Radiography Measurements of Projected Mass Density Distribution*

X-ray radiography measurements were taken by project partners at Argonne National Laboratory. The path-integrated liquid fuel mass distribution, namely the projected density, is measured using this technique [2, 3]. Measurements of the time-resolved projected density of the fuel sprays were conducted at the 7-BM beamline of the Advanced Photon Source [4, 5]. Each diesel injector was mounted horizontally in a high-pressure spray chamber fitted with a pair of x-

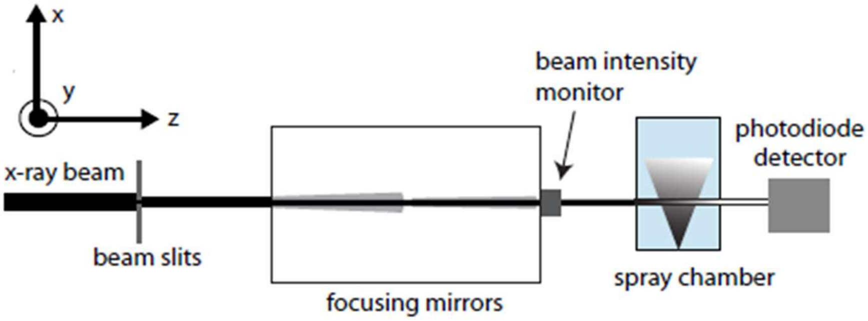

Figure 4: Schematic of the x-ray radiography measurement setup at Argonne National Lab.

ray transparent windows [4, 6, 7]. The chamber was held at room temperature and pressurized with nitrogen which was continuously purged the vessel to inhibit droplet accumulation.

Figure 4 shows a schematic of the radiography diagnostic setup. The x-ray source is from the APS at Argonne and the photodiode detects the outgoing x-ray beam intensity. A beam of x-rays from the bending magnet source passed through a double crystal monochromator and beam defining slits to create a monochromatic x-ray beam at 8 keV (4.3% bandwidth) [4, 6, 7]. The x-rays were focused to a 4 μm x 6 μm pencil beam with a pair of x-ray focusing mirrors. The incident radiation, I_o, was measured with an intensity monitor before the x-rays impinged on the spray. The attenuated intensity, I, was captured with a photodiode [4]. At 8 keV x-ray energy, the main interaction of the photons with the fuel spray is through photoelectric absorption. As the beam passes through the spray, photons are absorbed by the fuel. The effective path length, l, can be calculated using the Beer-Lambert law:

$$l = \frac{1}{\mu} \ln\left(\frac{I_o}{I}\right) \tag{3}$$

where μ is the linear attenuation coefficient of the fuel, found through calibration. If the fuel density, ρ, is known, the path length can be converted into the projected fuel density, $\bar{M}$ (units μg/mm^2), through the relation

$$\bar{M} = \rho l \tag{4}$$

To create a 2D map of the fuel spray distribution, the spray chamber was traversed both horizontally and vertically about a fixed beam, and the x-ray intensity was measured at a raster grid of points. To increase the signal-to-noise ratio, between 16 to 32 spray events were averaged at each spatial location. The radiography measurements were time averaged from 1.3 to 2.3 ms, so the steady portion of the spray is analyzed.

4.1.4 Argonne Experiments: Ultra-Small Angle X-ray Scattering (USAXS) Measurements of Sauter Mean Diameter (SMD)

Ultra-Small Angle X-ray Scattering (USAXS) measurements were conducted by project partners at Argonne National Laboratory to quantify drop sizes within optically-dense regions of diesel sprays (e.g., along the spray centerline). USAXS measurements were obtained by Argonne National Laboratory at the 9-ID beamline of the Advanced Photon Source. A 100x500 μm x-ray beam is passed through the spray, with resultant x-ray scattering, I_{scat}, detected as a function of the scattering angle to determine the differential scattering cross section of the sampled region, which can then be related to the total surface area per volume of the sample. If the total droplet volume in the sample can be determined (such as with x-ray radiography measurements of projected density), the *SMD* of the system can be determined. More detail regarding the theory underpinning the USAXS measurements can be found in [8]. Uncertainty in the measurements is estimated to be 6% of the reported value due to noise in the x-ray radiography and scattering measurements and relative positioning errors between the measurements.

4.1.5 Experimental Conditions

The experiments in this project were executed in three phases; each phase sought to improve the diagnostic setup used in the previous campaign and to reduce measurement uncertainties. Table 3 provides a summary of experimental conditions for each phase of the project.

Table 3: Summary of experimental campaigns conducted over the course of this project

	Injector	Light Source	Ambient Density	Injection Pressure	Injector Orientation	Objective
Phase I	Spray D #209133	White LED	1.2, 2.4, 22.8 kg/m^3	50, 150 MPa	0°	To develop the SAMR processing steps
Phase II	Spray A #306020	Red LED 633 nm	22.8 kg/m^3	50, 100, 150 MPa	0°	To improve the light source and use a smaller nozzle size
Phase III	Spray D #209133	Red LED 633 nm	1.2, 5.8 kg/m^3	50, 150 MPa	90, 120, 165°	To improve the DBI setup, reduce the SNR in radiography, to assess the asymmetries in the spray

4.2 Model Formulation and Validation (SOPO Task 2 and Task 3)

4.2.1 Turbulence-Induced Breakup in Diesel Sprays

Several theories have been put forth to explain the role of nozzle-generated turbulence on the primary breakup process [23, 24, 25, 26, 27]. Schweitzer proposed that turbulence generated in the nozzle serves to augment the aerodynamic breakup process [25]. This theory was evaluated by examining images of fuel jet breakup conducted by Lee and Spencer [28], as shown in Figure 5, and Schweitzer [25] into evacuated and pressurized chambers across a range of liquid Reynolds numbers ($Re_f \sim 1500 - 9000$). Schweitzer found that complete atomization of the jet

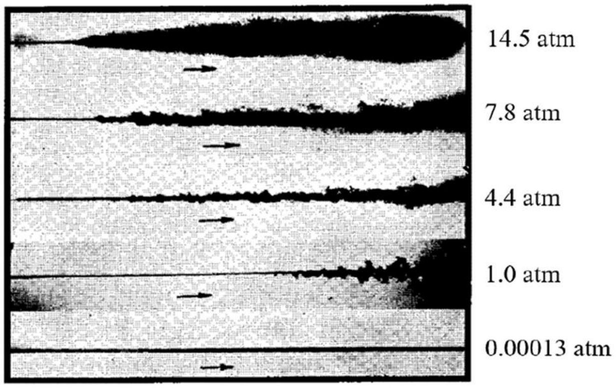

Figure 5: Photographs detailing the effect of ambient pressure on fuel jet breakup, modified from Lee and Spencer [28].

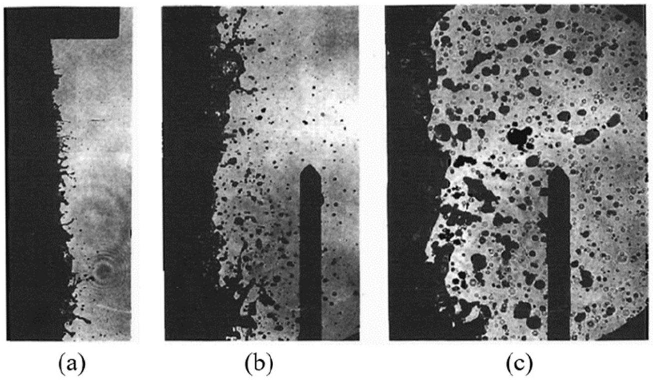

Figure 6: Pulsed shadowgraphs near the liquid-gas interface of a low-velocity water jet [50] (a) at the nozzle exit and at distances of (b) 10 and (c) 50 nozzle diameters from the nozzle exit.

could be suppressed if the spray was injected into rarefied gas or if the nozzle exit conditions of the jet were laminar. These results led to the hypothesis that the radial component in turbulent pipe flow could cause disturbances on the surface of the jet beyond the nozzle exit, which then grow according to aerodynamic wave growth. However, without sufficient spatial and temporal resolution of their imaging set-up to characterize the length and time scales of the primary atomization process, the proposed theory could not be directly validated. In spite of this, this conceptual framework forms the foundation for the majority of existing turbulence-induced breakup models used to study diesel spray formation.

Due to advancements in imaging technology since the work of Schweitzer, Faeth and co-workers were able to propose and validate a phenomenological model for turbulence-driven spray atomization using pulsed shadowgraphy, as shown in Figure 6, and high-magnification holographic imaging [23, 27, 29, 30]. Wu and coworkers postulated that droplets formed from turbulent breakup were due to turbulent kinetic energy overcoming the surface tension energy at the liquid-gas interface. This hypothesis was tested by systematically isolating the influence of turbulence induced breakup from other known breakup mechanisms, such as cavitation through careful design of the injection system, and aerodynamics by injecting into relatively low ambient density environments. By injecting into conditions where the liquid-to-gas density ratio (ρ_f/ρ_g) was large, the magnitude of inertial forces acting on the jet were expected to be minimized. For (ρ_f/ρ_g) greater than 500, aerodynamic effects were observed to be diminished and have little effect on the droplet formation process. It was hypothesized that because droplet-forming eddies only needed enough turbulent kinetic energy to surpass the surface energy present at the liquid-gas interface, initially formed droplet sizes, SMD_i, should only scale with jet properties at the nozzle exit. Indeed, analysis of the experimental images confirmed that SMD_i scaled with We_f alone [29],

$$\frac{SMD_i}{d_j} = 77We_{f_{dj}}^{-0.74} \tag{5}$$

where d_j is the injector nozzle diameter. In comparison to length scales characterizing the turbulence spectrum, *SMD*i was found to be larger than estimated Kolmogorov length scales, but smaller than integral length scales. As a result, Faeth and coworkers hypothesized that because turbulent eddies formed in the injector convect downstream and dissipate energy while doing so, the reduced size of droplet-forming eddies, l_i, likely exist within the inertial sub-range of the turbulence spectrum. This hypothesis is supported by the scaling of SMD_i in Equation 1.8, which is dependent on both the dimension and velocity of the flow.

However, the size of ligaments and droplets were observed to be influenced by aerodynamic effects when the spray was injected into (ρ_f/ρ_g) conditions less than 500. Wu and co-workers proposed that aerodynamic effects can enhance the spray breakup process by reducing the enery required to form a droplet. As schematically represented in Figure 1.13 [23], acceleration of gas over a ligament can reduce the local pressure, akin to flow over a sphere [31]. Faeth and co-workers modeled the enhanced aero-dynamic effects as a mechanical energy, $C_{sa}\rho_g\overline{U}_o^2 l_i^3$, which together with the kinetic energy from the turbulent velocity fluctuations, $\rho_f v_{li}^2 l_i^3$, balances the surface energy, $C_{si}\sigma l_i^2$, at the instant of droplet formation, as mathematically defined below,

$$\left(\rho_f v_{li}^2 + C_{sa}\rho_g\overline{U}_o^2\right)l_i^3 = C_{si}\sigma l_i^2 \tag{6}$$

where v_{li} is the radial velocity of an eddy of size l_i, $\overline{U}_o$ is the average jet exit velocity, and C_{sa} and C_{si} are coefficients that incorporate the effects due to ellipticity, nonuniform pressure variation over the ligament surface and non-uniform velocities within the eddy. Even under conditions where aerodynamics augmented the spray breakup process, the size of droplet-forming eddies, l_i, were still found to scale with eddies within the inertial subrange of the turbulence spectrum.

Through evaluation of images characterizing the formation of ligaments and the resultant droplets for fully-developed turbulent jets across a wide range of liquid-togas density ratio ($\rho_f/\rho_g \sim 104 - 6230$), Reynolds number ($Re_f \sim 1.5\cdot10^5 - 5.3\cdot10^5$) and Weber number ($We_f \sim 7\cdot10^4 - 4.1\cdot10^5$) conditions, three different primary breakup regimes were identified, as depicted in Figure 1.14. Non-aerodynamic primary breakup is found to occur for high (ρ_f/ρ_g) conditions where aerodynamic effects are suppressed, and turbulence is the only mechanism driving the formation of droplets. Transition between non-aerodynamic (turbulent) and aerodynamically enhanced primary breakup was determined to be a function of (ρ_f/ρ_g) alone. The critical (ρ_f/ρ_g) condition defining this transition was proposed to be 500, although Wu and Faeth acknowledged that more experimental work was needed to better define the breakup regime boundaries [23]. Within the aerodynamically enhanced breakup regime, turbulence is the primary mechanism governing the spray formation process, although aerodynamics serves to reduce the energy required to form droplets. As a result, smaller primary droplets are observed within this regime relative to ones formed in the non-aerodynamic regime.

For (ρ_f/ρ_g) conditions less than 500, Wu and Faeth hypothesized that for sufficiently large enough injection velocities, the secondary droplet breakup process would become so fast that the primary and secondary breakup processes would become effectively merged and indistinguishable from one another [23]. Under such conditions, the measured droplet sizes were thought to be highly influenced by aerodynamic secondary breakup processes. The transition between aerodynamically enhanced and merged aerodynamic primary and secondary breakup regimes was defined using the relative timescales of ligament formation to secondary breakup timescale ratios (τ_r/τ_b), where the critical timescale ratio was selected to be 4. In contrast to the non-aerodynamic primary breakup regime, measured droplet sizes in the aerodynamic primary

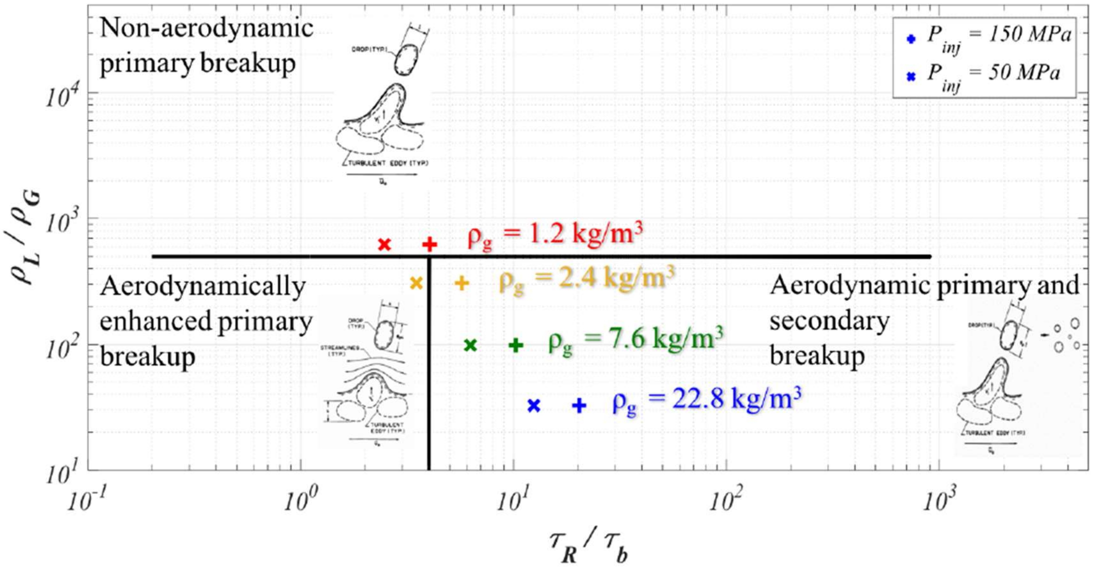

Figure 7: Turbulent primary breakup regime map, adapted from the work of Faeth and co-workers [23].

and secondary breakup regime are smaller and have a strong dependence on the secondary breakup mechanism.

Although the phenomenological framework developed by Faeth and co-workers to explain the role of turbulence in the primary atomization process is strongly supported through comparison with direct observation and measurements, questions remain about the applicability of these findings to sprays formed from practical diesel injectors. The set of experimental data supporting their theory considers jets issued from large idealized nozzles, with nozzle diameters ranging from 3.6 - 9.5 mm and with long enough nozzle L/d_j to ensure fully developed turbulence conditions at the nozzle exit. In general, diesel injectors utilize nozzles with small diameters and short length-to-diameter ratios, typically with $d_j < 1$ mm and $L/d_j < 12$ [32]. However, results from Wu and co-workers suggest that for conditions where aerodynamic forces have a minimal influence on the spray ($\rho_f/\rho_g > 100$), the condition at the onset of turbulent breakup and the size of primary and secondary droplets were relatively independent of L/d_j [30]. Therefore, discrepancies between the L/d_j of diesel injectors and those considered by Faeth and co-workers in the development of their primary breakup regime diagram may not affect the applicability of their results to diesel sprays.

However, as noted by Dumouchel [33], divergent conclusions in the literature regarding the role of turbulence in the spray breakup process are possibly related to the size of nozzles used in the various experimental campaigns [23, 34, 35]. Karasawa and co-workers [34] and Tamaki and co-workers [35] considered sprays formed from small nozzles ($d_j \sim 300\ \mu$m) with high injection velocities (90 - 220 m/s). Their experimental results suggest that increasing turbulence in cavitation free jets did not particularly promote atomization. These results directly conflict with the work of Faeth and co-workers [19, 48, 50, 51]. However, as previously mentioned, their experimental data considers sprays formed from relatively larger nozzles ($d_j > 3.6$ mm) with slower injection velocities ($U_{inj} \sim 16 - 67$ m/s). As a result, it is still an open research question if the conclusions from Faeth and co-workers regarding the role of turbulence in the primary atomization process can be directly applied to diesel sprays.

Using the regime diagram from Wu and Faeth shown in Figure 7, a set of experimental conditions was defined to explore the applicability of the theories underpinning the three primary breakup regimes to diesel sprays. The project also employed well-characterized research-grade diesel injectors that are known to suppress cavitation phenomena within the nozzle from the ECN, while a range of injection and ambient conditions were selected to systematically explore the role of areodynamics and turbulence on the diesel spray formation process. As shown in Figure 7, the most influential parameters for determining the pertinent breakup regime are the ambient gas density and the fuel injection pressure.

Based on the work of Wu and Faeth, we targeted experiments for model validation at conditions that translated through the regimes identified Figure 7. Sprays were injected into ambient densities characterizing conventional diesel conditions ($\rho_g > 7.6\ kg/m^3$) to assess the use of models that include a joint contribution of aerodynamics and turbulence on the atomization process, whereas sprays at atmospheric conditions ($\rho_g \sim 1.2\ kg/m3$) enabled assessment of purely turbulence-induced breakup models. As shown in Figure 7, modulation of the fuel injection pressure (injection velocity) enabled further translation across the Wu and Faeth regime diagram.

4.2.2 Proposed Turbulent Breakup Model (KH-Faeth)

In this section, we describe the formulation of a new spray model that incorporates the physics of turbulent breakup, as studied and quantified by Faeth and co-workers (e.g., [23, 29, 30]). We benchmark the proposed model against the widespread computational standard Kelvin-Helmholtz (KH) aerodynamic breakup model [38].

In order to understand the sensitivity of the predicted spray structure is to the representation of the turbulence-induced breakup process, a new hybrid primary atomization model, called the KH-Faeth model, was developed. The KH-Faeth model was developed from the KH-ACT modeling framework [37], where the competition between aerodynamic and turbulent breakup mechanisms on the primary atomization process is treated identically. However, in the KH-Faeth model, the turbulent breakup length and time scales are modeled using empirical correlations from the work of Faeth and co-workers [23]. The salient conclusions of their work that support their correlation are highlighted here.

Based on an extensive database of near-nozzle holography imaging measurements across a wide range of Re_f ($9\text{x}10^4$ - $5.3\text{x}10^5$) and (ρ_f / ρ_g) (104-6230) conditions, Faeth and co-workers developed a phenomenological framework to describe the onset of turbulent breakup and subsequent droplet formation process for round turbulent liquid jets injected into quiescent gases. For liquid jets injected into atmospheric conditions, they found that breakup scaled purely with the nozzle exit turbulence properties. However, for (ρ_f / ρ_g) less than 500, they found that aerodynamic effects can enhance spray breakup. They hypothesized that this enhanced breakup occurs due to a local reduction in pressure due to acceleration of the ambient gas over surface protuberances that originate from liquid turbulence, akin to flow over a sphere [23]. Note that this mechanism of aerodynamically-enhanced breakup is distinct from the aerodynamically-induced breakup mechanism of surface wave development and growth that is represented in the KH breakup model. Using an energy balance between the mechanical energy at the liquid surface due to aerodynamic effects, the kinetic energy from the turbulent velocity fluctuations, and the surface energy at the instant of droplet formation, it was found that the measured size of ligaments and droplets formed, L_{Faeth}, were of the same order as estimated eddy scales within the inertial sub-range of the turbulence spectrum. It should be noted that this correlation will therefore result in the formation of droplets that are smaller than those predicted by the KH-ACT model, since in the KH-ACT model, the turbulent length scale is assumed to be proportional to the integral length scale.

Based on their analysis of the measured liquid surface ligament and droplet properties

at the onset of turbulent breakup, the time required to form a droplet, τ_{Faeth}, was found to be proportional to the time required for a droplet to form from a ligament of size L_{Faeth}, according to the Rayleigh instability mechanism. For low Ohnesorge liquids, where viscosity effects can be neglected, Wu and Faeth [29] determined that $\tau_{Faeth} \propto \sqrt{\rho_f (L_{Faeth})^3/\sigma}$. In the KH-Faeth model, a similar definition is implemented for τ_{Faeth}:

$$\tau_{Faeth} = C_\tau \sqrt{\rho_f \frac{L_{Faeth}^3}{\sigma}} \tag{7}$$

where C_τ is the turbulent breakup time constant, and σ is the surface tension of the liquid in the ambient gas. In the present study, C_τ is assumed to equal unity. Wu and Faeth also developed a correlation to relate L_{Faeth} to nozzle exit turbulence properties and the axial location, x, where droplets are formed from the turbulent breakup process [23]. By assuming that the stream-wise velocity of the droplet-forming eddy remains relatively constant and can be equated to the injection velocity, U_{inj}, x is simply equal to the product of U_{inj} and τ_{Faeth}. By using Equation 5.1 and re-arranging the terms, L_{Faeth} can be determined with the following relation:

$$\frac{L_{Faeth}}{\Lambda} = C_{sx} \left(\frac{x}{\Lambda We_{f\Lambda}^{1/2}} \right)^{2/3} \tag{8}$$

where Λ is the radial integral length scale, C_{sx} is an empirical constant, and $We_{f\Lambda}$ is the Λ-based liquid Weber number, $\rho_f U_{inj}^2 \Lambda/\sigma$. Based on experimental data across a wide range of Re_f ($9 \cdot 10^4 - 5.3 \cdot 10^5$) and ($\rho_f/\rho_g$) (104-6230) conditions, Wu and Faeth determined that the empirical correlation in Equation 5.2 best fit the entire experimental data set when C_{sx} was set to 0.65. As a result, this relation is capable of representing the size of droplets formed across the non-aerodynamic and aerodynamic breakup regimes proposed by Wu and Faeth [23], as schematically shown in Figure 1.14.

In the KH-Faeth model, τ_{Faeth} and L_{Faeth} are used to represent the characteristic time and length scale governing the turbulence-induced primary breakup process. The turbulence-induced breakup model is implemented in a construct similar to the KH-ACT model. At each time step, only one primary atomization mechanism, either KH or turbulence-induced breakup, is assumed to act upon the computational parent parcel. KH and turbulent primary breakup rates are calculated and compared, and the maximum breakup rate is selected as the dominant primary atomization mechanism, as mathematically defined below,

$$\frac{L_A}{\tau_A} = max\left\{\frac{a - r_c}{\tau_{KH}}, \frac{L_{Faeth}}{\tau_{Faeth}}\right\} \tag{9}$$

Similar to the KH-ACT atomization model, if KH primary breakup is dominant, then the parent parcels evolve according to:

$$\frac{da}{dt} = \frac{a - r_c}{\tau_{KH}} \tag{10}$$

$$\tau_{KH} = \frac{3.726 B_1 a}{\Lambda_{KH} \Omega} \tag{11}$$

$$r_c = B_o \Lambda_{KH} \tag{12}$$

where τ_{KH} is the characteristic breakup time, and Ω and Λ_{KH} are the maximum growth rate and corresponding wavelength of the most unstable liquid surface wave, as numerically solved from linearized stability theory [36]. However, if turbulent primary breakup dominates the atomization process, then the parent parcel decreases in size according to:

$$\frac{da}{dt} = -C_{T,CAV} \frac{L_A}{\tau_A} \tag{13}$$

where $C_{T,CAV}$ is equal to unity.

After a child droplet has been formed from the selected primary atomization process, the droplet may undergo subsequent secondary droplet breakup due to the KH instability if the droplet size is larger than Λ_{KH}.

Based on an extensive modeling study by Magnotti [39], the model is implemented according to (ρ_f / ρ_g) regimes similar to those identified by Faeth and co-workers in Figure 7.

Non-Aerodynamic Primary Breakup Regime

Conditions Defining Boundary of Regime: $(\rho_f / \rho_g) \geq 300$

Primary Breakup: Turbulent mechanism in isolation determines predicted breakup rate at each time instant for an individual computational parcel.

Droplet Size [23]: $\frac{L_{Faeth}}{\Lambda} = C_{sx} \left(\frac{x}{\Lambda We_{f\Lambda}^{1/2}} \right)^{2/3}$

Breakup Time [23]: $\tau_{Faet} = C_{\tau} \sqrt{\rho_f \frac{L_{Faeth}^3}{\sigma}}$

Secondary Breakup: Neglected

For conditions where (ρ_f / ρ_g) > 300, non-cavitating diesel sprays are proposed to undergo non-aerodynamic primary breakup. The size of primary droplets formed from this process are hypothesized to be determined by the characteristic length scale of turbulent eddies with sufficient energy to overcome surface tension energy at the liquid-gas interface. This characteristic turbulent length scale is defined using the empirical correlations developed by Wu and Faeth [23]. The time required to form a droplet, τ_{Faeth}, scales with the time required for a droplet to form from a ligament of size L_{Faeth}, according to the Rayleigh instability mechanism. Comparison of model predictions against *SMD* measurements along the spray centerline did not indicate a strong influence of secondary droplet breakup [39]; as a result, secondary breakup is not recommended to be included.

Merged Aerodynamic Primary and Secondary Breakup Regime

Conditions Defining Boundary of Regime: (ρ_f / ρ_g) < 300

Primary Breakup: Either aerodynamic or turbulent mechanism dictates the primary atomization process at each time instant for an individual computational parcel, based on the mechanism with the fastest predicted breakup rate.

Turbulent Primary Breakup [23]:

Droplet Size: $\frac{L_{Faeth}}{\Lambda} = C_{sx}\left(\frac{x}{\Lambda We_{f\Lambda}^{1/2}}\right)^{2/3}$

Breakup Time: $\tau_{Faeth} = C_{\tau}\sqrt{\rho_f \frac{L_{Faet}^3}{\sigma}}$

Aerodynamic Primary Breakup [38]:

Droplet Size: $r_c = B_o \Lambda_{KH}$

Breakup Time: $\tau_{KH} = \frac{3.726 B_1 a}{\Lambda_{KH}\Omega}$

Secondary Breakup [38]:

Droplet Size: $r_c = B_o \Lambda_{KH}$

Breakup Time: $\tau_{KH} = \frac{3.726 B_1 a}{\Lambda_{KH}\Omega}$

For conditions where (ρ_f / ρ_g) < 300, the primary breakup process for non-cavitating diesel sprays is proposed to be governed by both aerodynamic and turbulence-induced breakup mechanisms. As formulated in the new KH-Faeth spray model, competition between aerodynamic and turbulent breakup mechanisms drives the droplet formation process and is hypothesized to be determined by the mechanism with the fastest predicted breakup rate. To allow for continuous spray breakup behavior across the two regimes, the turbulent breakup process is modeled consistently with the formulation within the non-aerodynamic primary breakup regime, using the empirical correlations from Wu and Faeth [23] for L_{Faeth} and τ_{Faeth}, as defined above. The aerodynamic breakup process is modeled using the KH spray model formulation from Beale and Reitz [38], where a primary droplet of size r_c is formed in a breakup timescale of τ_{KH}.

4.2.3 Computational Model Setup in OpenFOAM

The open-source CFD code, OpenFOAM, was employed to model the injection of an n-dodecane spray into a constant volume chamber. For the ambient gas, continuum-phase turbulence flow was modeled by Reynolds-Averaged Navier-Stokes (RANS) coupled with a standard k-ε turbulence model. The computational mesh is based on the experimental facilities used for spray measurements at Argonne [2] and Georgia Tech [42], where an isolated fuel spray is injected from an axially-drilled fuel injector into a large quiescent test chamber volume (1 – 2 L). For these environments, the wall effects are likely insignificant; as a result, a cubic computational domain 100mm in length was selected to model a free liquid jet. The computational domain was initialized with 4-mm static hexahedral structured grid. Then, a run-time based dynamic mesh refinement was applied to allow CFD mesh size reductions to a minimum grid size of 0.25 mm to improve prediction accuracy. One million computational parcels were consecutively introduced into the computational domain over the injection duration of 2.5 ms. Time-averaged drop sizing solutions were obtained through 1 ms after the start of injection, where drop sizing statistics had converged. The measured fuel mass flow rate (http://www.sandia.gov/ECN) and nozzle discharge coefficient were used to calculate the injection velocities at the nozzle exit, with the rate of injection profile generated by a virtual injection rate calculator [40].

4.2.4 Summary of Model Validation Simulations

Model validation experiments were executed using non-cavitating *n*-dodecane fuel injections with the ECN Spray A and Spray D injectors [41]. Both Spray A and Spray D are axially-drilled single-hole diesel injectors with well-characterized internal nozzle geometries that are demonstrated to suppress cavitation.

To validate the proposed KH-Faeth model, two classes of non-reacting test conditions; i) vaporizing spray and ii) non-vaporizing spray, are considered in this study as listed in Table 4. Under non-vaporizing conditions, a wide range of ambient gas density conditions are defined to examine the model predictive ability over a range of different primary breakup regimes (Figure 7). Vaporizing conditions were included in the test matrix to assess model accuracy using more widely-accepted spray model validation metrics like the liquid and vapor penetration rate.

Table 4: Experimental conditions used for spray model validation simulations.

ECN injector (serial #)	Spray A (210675)	Spray D (209133)
Orifice diameter [μm]	89.4	186
Discharge coefficient	0.86	0.9
Nozzle K-factor	1.5	3.7
Ambient gas temperature [K]	303 (non-vaporizing) 900 (vaporizing)	303 (non-vaporizing) 800 (vaporizing)
Ambient gas composition [% by volume]	N_2: 89.71% CO_2: 6.52% H_2O: 3.77 %	N_2: 100%
Ambient gas density [kg/m^3]	22.8	1.2 / 2.4 / 22.8
Nominal ambient gas pressure [bar]	60	1 / 2 / 20
Liquid/gas density ratio [-]	33.7	674 / 337 / 33.7
Injection pressure [bar]	1500	500 / 1000 / 1500

5 Project Results

5.1 Development of Scattering-Absorption Measurement Ratio (SAMR) Diagnostic for Drop Sizing in Diesel Sprays

5.1.1 Theoretical Development of SAMR Diagnostic

A new measurement diagnostic was developed in this project to quantify drop size distributions in diesel sprays at engine-relevant conditions. This diagnostic combines optical thickness measurements conducted at GA Tech with projected mass density measurements conducted at Argonne, to yield the scattering-absorption measurement ratio (SAMR), which is proportional to the average droplet diameter within the measurement probe volume. Here, we demonstrate the theoretical basis of the SAMR diagnostic.

Extinction or optical thickness, τ, is quantified by measuring the attenuation of an incident illumination source (I/I_0) as it passes through a cloud of spherical droplets [9]:

$$\frac{I}{I_o} = e^{-\tau} \tag{14}$$

The optical thickness, τ, can be related to the characteristics of the droplet field via the Mie solution to Maxwell's equation, which provides an analytical solution for the 3-D scattering and absorption behavior for a light wave interacting with a spherical object. Following Mie-theory:

$$\tau = \alpha_{ext} z \tag{15}$$

where, α_{ext}, is the attenuation coefficient and, z, is the illumination path-length through the droplet field. For a dispersion of droplet sizes within the probed cloud, the attenuation coefficient can be expressed as:

$$\alpha_{ext} = \sum_j C_{ext,j} \cdot (N/V)_j = \frac{1}{V}\sum_j C_{ext,j} N_j \tag{16}$$

where, $(N/V)_j$, is the number of droplets of diameter d_j normalized by the measurement probe volume, V, defined by the laser path volume through the spray. $C_{ext,j}$ is the corresponding extinction cross section for drops of size j, proportional to the geometric cross-sectional area d_j^2. The expression for optical thickness can be simplified when there is a dispersion of droplet sizes by introducing the number-weighted mean extinction cross section, $\overline{C_{ext}}$:

$$\overline{C_{ext}} = \sum_j \frac{C_{ext,j} \cdot N_j}{N} = \frac{1}{N}\sum_j C_{ext,j} N_j \tag{17}$$

Thus, the attenuation coefficient can be expressed as the product of the number-weighted mean extinction cross section and the number density of all droplets in the probed volume, (N/V):

$$\alpha_{ext} = \overline{C_{ext}} \cdot (N/V) \tag{18}$$

The total number density of droplets in the probed volume can also be expressed as a function of the liquid volume fraction, LVF, within the probed volume, and α_{ext} can be reformulated in terms of LVF:

$$LVF = \frac{V_{liq}}{V} = \frac{\sum_j N_j \cdot \left(\pi d_j^3/6\right)}{V} \tag{19}$$

$$\alpha_{ext} = \overline{C_{ext}} \frac{LVF \cdot N}{\sum_j N_j \cdot \left(\pi d_j^3/6\right)} \tag{20}$$

The expression for α_{ext} can be further simplified by introducing the number-weighted mean droplet volume, $\overline{\pi d^3/6}$, and substituting the relation into Equation (7):

$$\overline{\pi d^3/6} = \sum_j \frac{\left(\pi d_j^3/6\right) \cdot N_j}{N} \tag{21}$$

$$\alpha_{ext} = \frac{\overline{C_{ext}}}{\overline{\pi d^3/6}} \cdot LVF \tag{22}$$

Thus, a simplified expression for the attenuation coefficient, valid for a dispersion of droplet sizes in the probed droplet cloud is obtained. Substituting Equation (13) into Equation (6) shows τ as a function of LVF and d:

$$\tau = \alpha_{ext} z = \frac{\overline{C_{ext}}}{\overline{\pi d^3/6}} \cdot LVF \cdot z \tag{23}$$

For non-vaporizing isothermal conditions with constant ρ_f throughout the spray, the measurement of projected fuel density, $\bar{M}$, can also be recast as a measurement of LVF:

$$\bar{M} = \rho_f \frac{V_{liq}}{V} z = \rho_f (LVF) z \tag{24}$$

The ratio of the projected mass density and optical thickness measurements, Equations (14) and (15), respectively, can be shown to yield a quantity proportional to a number-weighted mean volume to surface area ratio, which is proportional to SMD:

$$\frac{\bar{M}/\rho_f}{\tau} \; \alpha \; \frac{LVF}{\tau} \; \alpha \; \frac{\overline{\frac{\pi d^3}{6}}}{\overline{C_{ext}}} \; \alpha \; \frac{\overline{d^3}}{\overline{d^2}} \; \alpha \; SMD \tag{25}$$

The measurement ratio $\bar{M}/\tau$ is referred to as the Scattering-Absorption Measurement Ratio (SAMR). The chosen terminology refers to the light-particle interaction regimes exploited by the diagnostic approach, where the optical thickness measurements are conducted with a visible illumination wavelength (633 nm) that is not absorbed by the fuel droplets, producing a pure scattering signal, and the projected mass density measurements are conducted with an x-ray source, where the signal is dominated by absorption of the illumination by the fuel droplets. To quantify the exact relationship between the measurement ratio and SMD of droplets within the measurement volume, the publicly available program MiePlot [10] is to model the predicted scattering signals (i.e., τ) for a given drop size distribution, probe volume, V, probe wavelength, λ (633 nm), and droplet refractive index, n (1.421 for n-dodecane).

As graphically depicted in Figure 8, the scattering cross section of a given droplet, C_{ext}, also depends on the collection angle of the laser detection optics ($\theta_{1/2}$). As the half collection angle, $\theta_{1/2}$, is increased, additional forward scattered light is detected, which serves to decrease the measured C_{ext}; for an increase in $\theta_{1/2}$ from approximately 0° to 5.6°, C_{ext} decreases by approximately 28%.

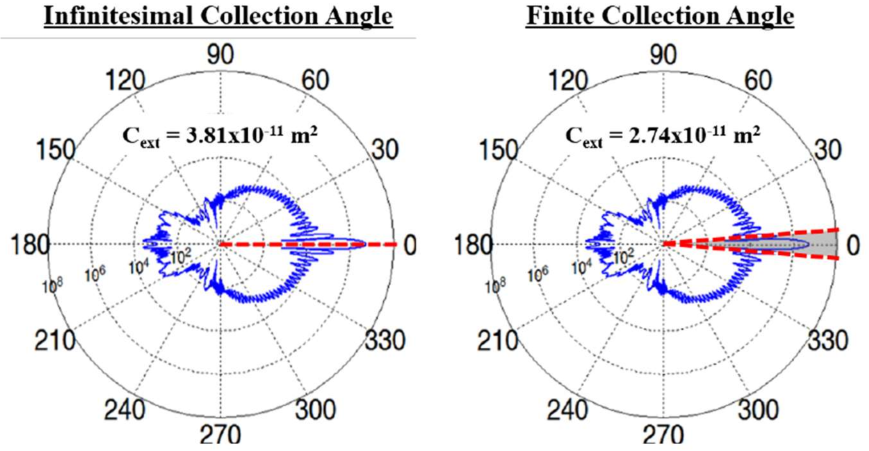

Figure 8: Calculated influence of measurement collection angle on collection of forward scattered light and measured C_{ext} from a 5 μm droplet. (a) $\theta_{1/2} = 0°$. (b) $\theta_{1/2} = 5.6°$. Simulations performed in MiePlot (λ = 633 nm, n = 1.421).

The scattering-absorption measurement ratio is then related to *SMD* by normalizing the calculated C_{ext} by $\overline{\pi d^3/6}$ for the assumed size distribution. This relationship is depicted in Figure 9, where a range of diesel-relevant *SMD* from 0.1 – 10 μm and geometric standard deviation, σ_g, from 1.0 - 1.75 of the assumed log-normal droplet size distribution is shown. This chart then serves as a lookup table of *SMD* for a given measurement ratio.

As shown in Figure 9, the droplet size distribution assumed in the determination of C_{ext} and $\overline{\pi d^3/6}$ has little effect on the relationship between the measurement ratio and *SMD* for droplets in the Mie-scattering regime. Thus, for simplicity, a monodisperse assumption (σ_g = 1.0) is

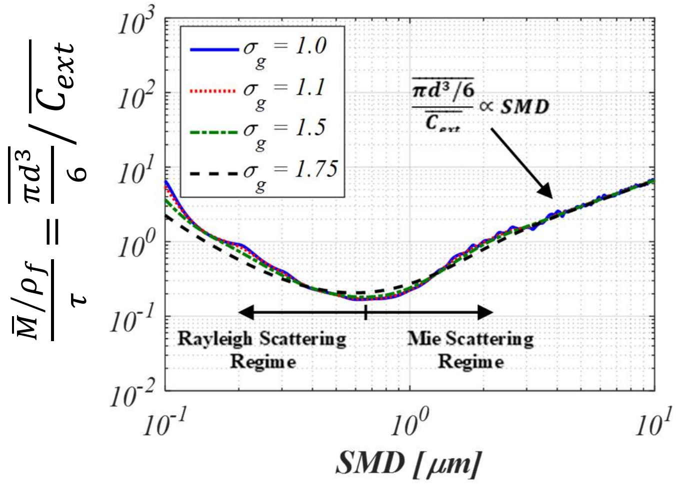

Figure 9: Scattering-Absorption Measurement Ratio (SAMR) as a function of *SMD* for various log-normal drop size distribution. Simulations performed in MiePlot (λ = 633 nm, n = 1.421).

employed in subsequent calculations. Figure 9 also shows that two possible *SMD* solutions exist for a given measurement ratio, one from the Mie-scattering regime and one from Rayleigh-scattering regime. In general, measurements in the literature indicate *SMD* values for diesel sprays that are greater than 1 μm [11, 12]. Thus, solutions in the Rayleigh-scattering regime are ignored and solutions for SMD are taken only from within the Mie-scattering regime.

5.1.2 SAMR Data Processing Demonstration

Because the measurement ratio requires two sets of data from two distinct experimental facilities, careful thought is required when jointly processing the two data sets. Researchers sought to minimize measurement uncertainties by keeping the experimental setups as consistent as possible. For example, the ambient densities and injection pressures were closely matched. The injectors were shared between the two laboratories. Commanded injection duration and fuel type was matched between the setups. The time average was taken from 1.3 to 2.3 ms for both data sets. It was also essential to ensure that equivalent measurement volumes and the same region of the spray were being compared for both facilities. Therefore, translational and rotational alignment of the sprays is important for jointly processing the two measurements.

Translational co-alignment of the two data sets was explored. It was studied whether the radial distributions of the data sets should be centered by:

- Shifting the data sets so that the peak value is aligned with x=0
- Centering the values equal to half of the peak around x=0 (full width half maximum, FWHM)

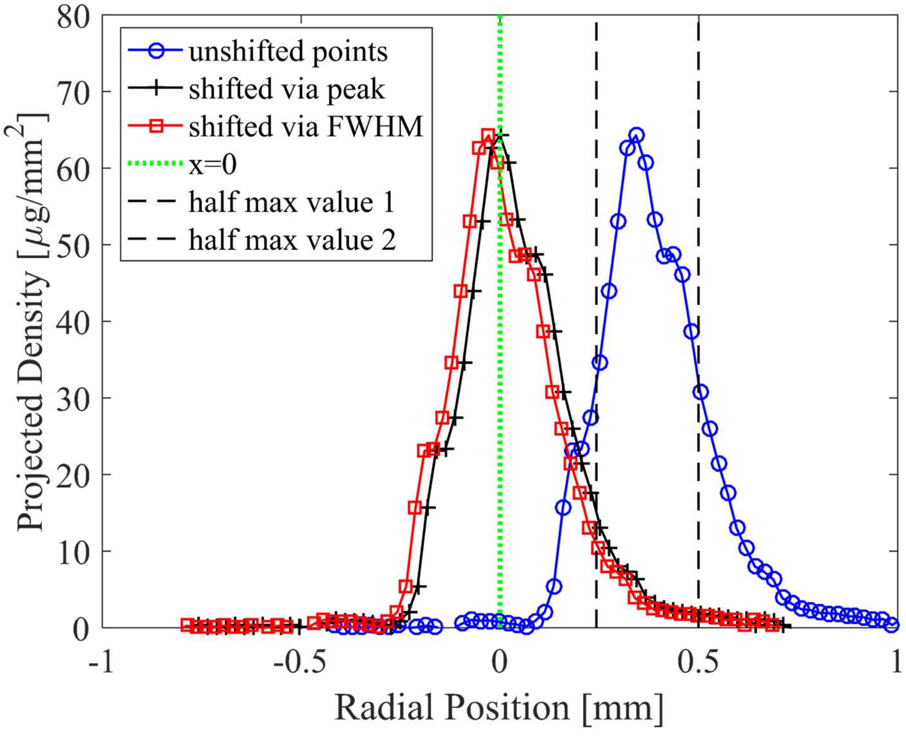

Figure 10: Projected density for Spray D 1.2 kg/m^3 50 MPa at an axial location of 16mm for the unshifted data, the data shifted according to the peak, and the data shifted via full width half maximum.

A study was conducted to analyze which of these methods was more accurate in confirming that the same area of the spray is being explored from both data sets [6]. Figure 10 shows an example of the projected density data aligned using method a) and method b). It appears that aligning the data via these two methods has a very small effect on the projected density data alone. Figure 11 shows that centering the radial distributions using the peak value is not an appropriate method for co-aligning the sprays from both facilities. The spray widths are different for each data set, so shifting the data sets using the full width half maximum method allows for the same region of the spray to be compared for both facilities.

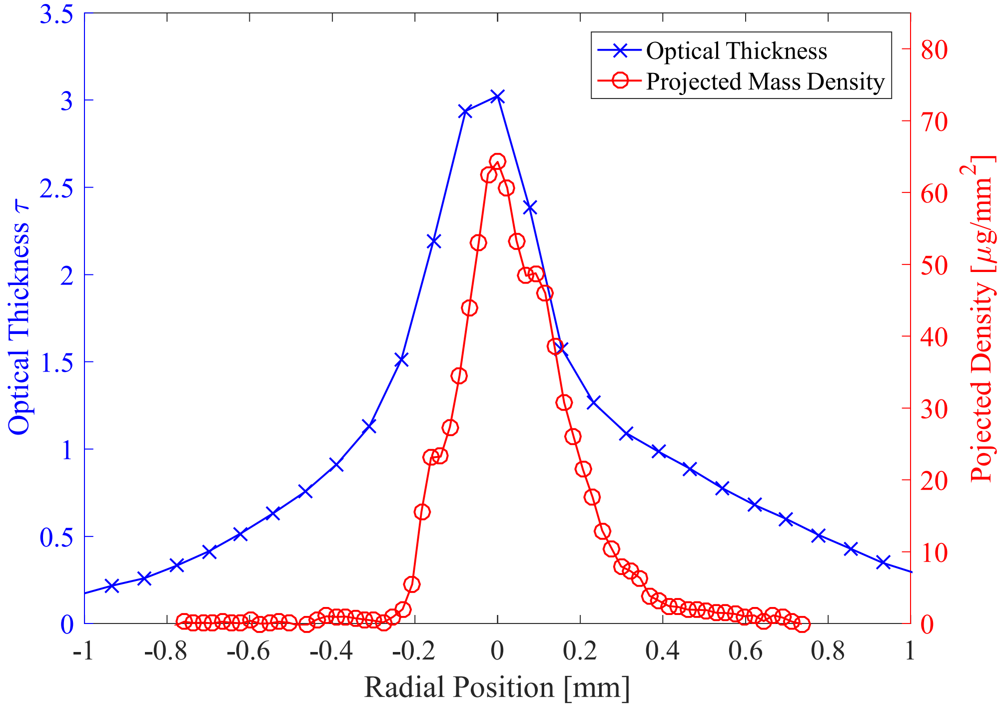

Figure 11: Projected density and optical thickness for Spray D 1.2 kg/m3 50 MPa at an axial location of 16mm using shifting according to the peak value.

Thus, translation co-alignment via full width half maximum is currently the method for ensuring that both data sets are aligned in the projected measurement plane. When aligning via this method, the values (optical thickness or projected density) that are equal to half the maximum are found. The center of the spray is defined as the midpoint between the half-maximum values on each side of the projected density and optical thickness distributions. The SAMR SMD results are determined assuming that these two midpoints correspond to the same location in the spray. Argonne also aligns the projected density data according to this method [13]. Figure 12 and Figure 13 show the unshifted and shifted optical thickness and projected density data sets for Spray D 1.2 kg/m^3 50 MPa at an axial location of 16 mm. Figure 14 shows the properly co-aligned data sets overlaid on one plot.

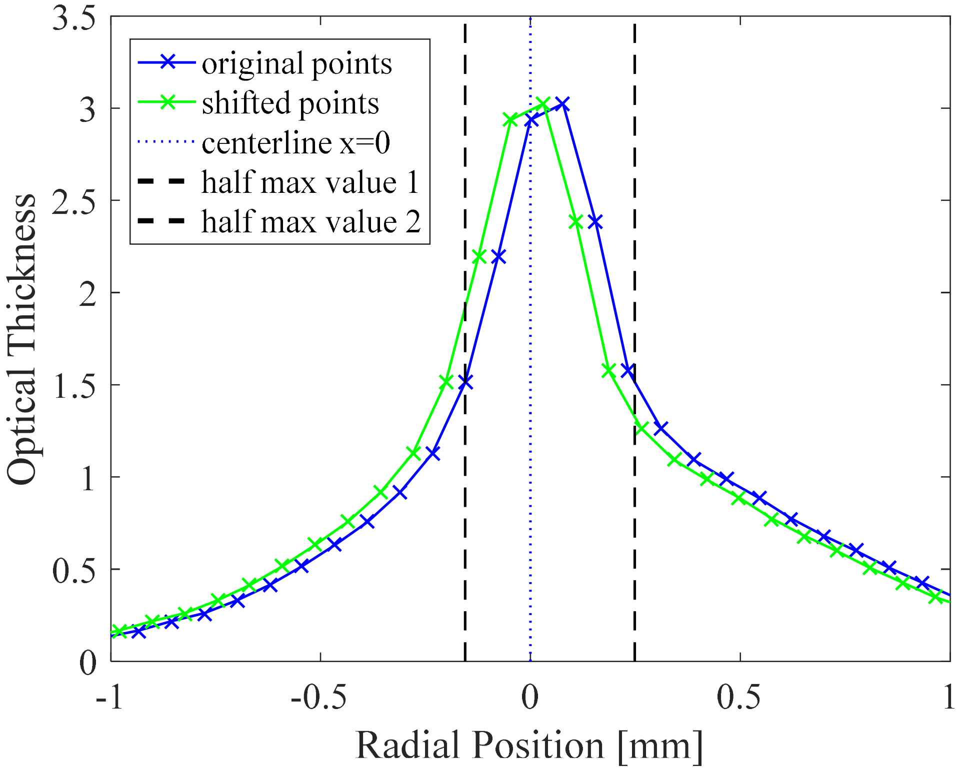

Figure 12: Optical thickness points for Spray D 1.2 kg/m3 50 MPa at an axial location of 16mm shifting according to the FWHM method.

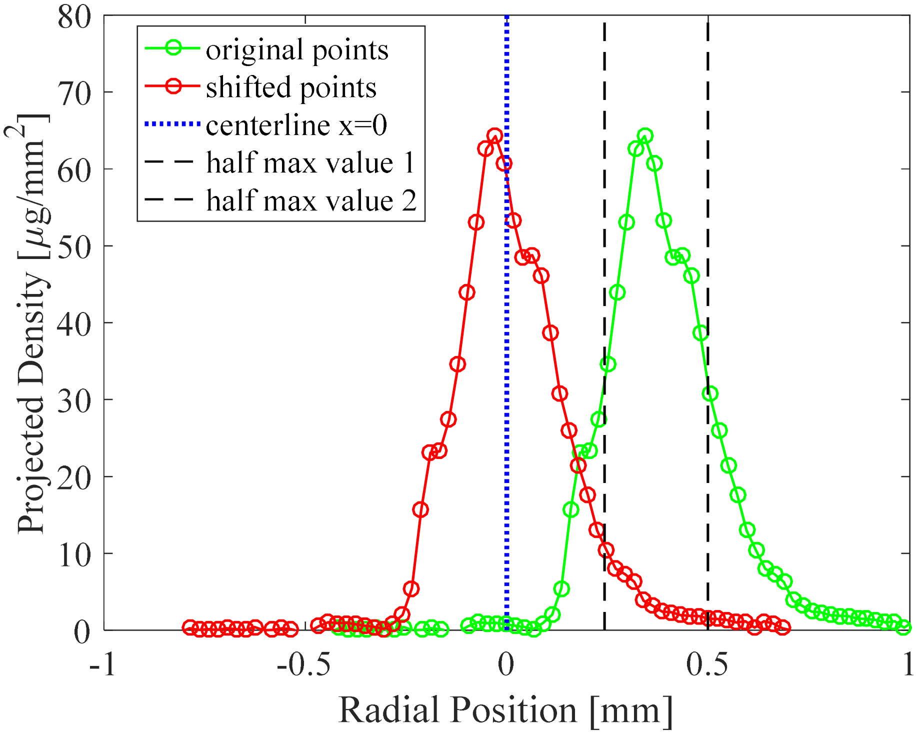

Figure 13: Projected density values for Spray D 1.2 kg/m3 50 MPa at an axial location of 16mm shifting according to the FWHM method.

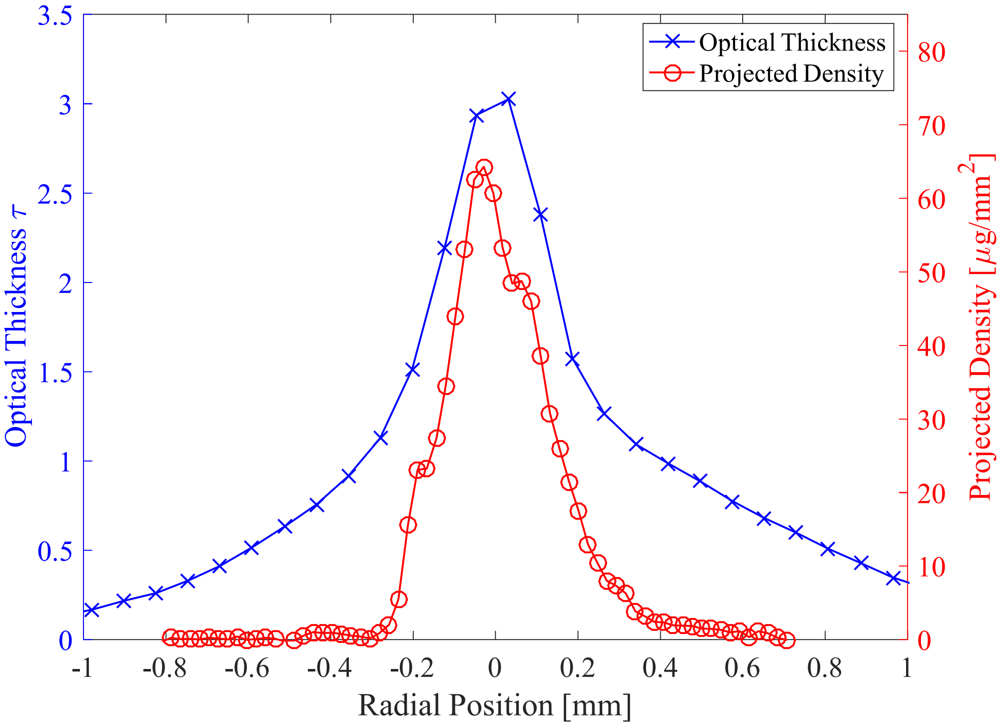

Figure 14: Both data sets overlaid for Spray D 1.2 kg/m3 50 MPa at an axial location of 16mm shifting according to the FWHM method.

In addition to translational co-alignment, the sprays also needed to be rotationally aligned. Previously, asymmetries in the spray were observed, which ultimately will have a large effect on the quantified SMD [4]. These asymmetries in the spray make it essential that the injectors are oriented in the same manner, so that the same region of the spray can be compared. For Phase I of the experimental campaign, the orientation between the two facilities was off by about 10°. For Phase II and III, the injector orientations were matched within approximately 1°. Table 3 provides a record of the aimed injector orientation for each condition. Figure 15 shows the ECN specifications for the 0° orientation.

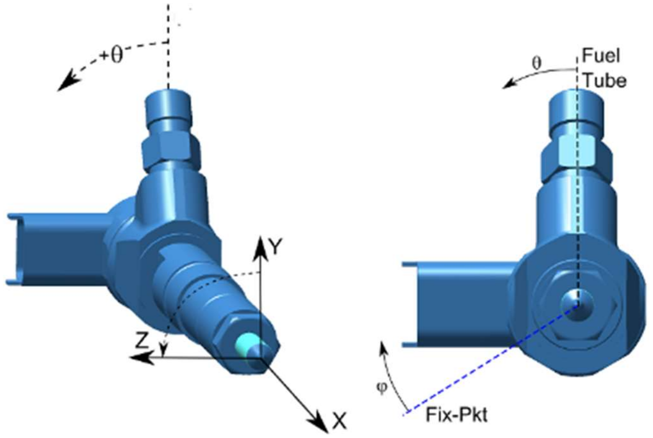

Figure 15: 0° orientation according to the ECN specifications.

After the two sprays were co-aligned, a resampling of the project density values occurred. Due to the nature of the radiography measurement, it is possible to achieve finer spatial resolution for the projected density data than the optical thickness data. The resolution of the optical thickness data was limited by the optical setup, namely by the projected pixel size. To ensure that the joint measurement analysis is conducted for equivalent measurement volumes, a resampling process was established. The resampled measurement volumes or bins are equal in size to the spatial resolution of the DBI measurements (see Table 2). Each bin is centered about each optical thickness point. The resampling process is illustrated in Figure 16. The dashed lines show the resampled measurement volumes. The green lines show the two limits for the SAMR technique. Finally, the purple boxes show the locations where the measurement ratio was considered valid for Phase 1.

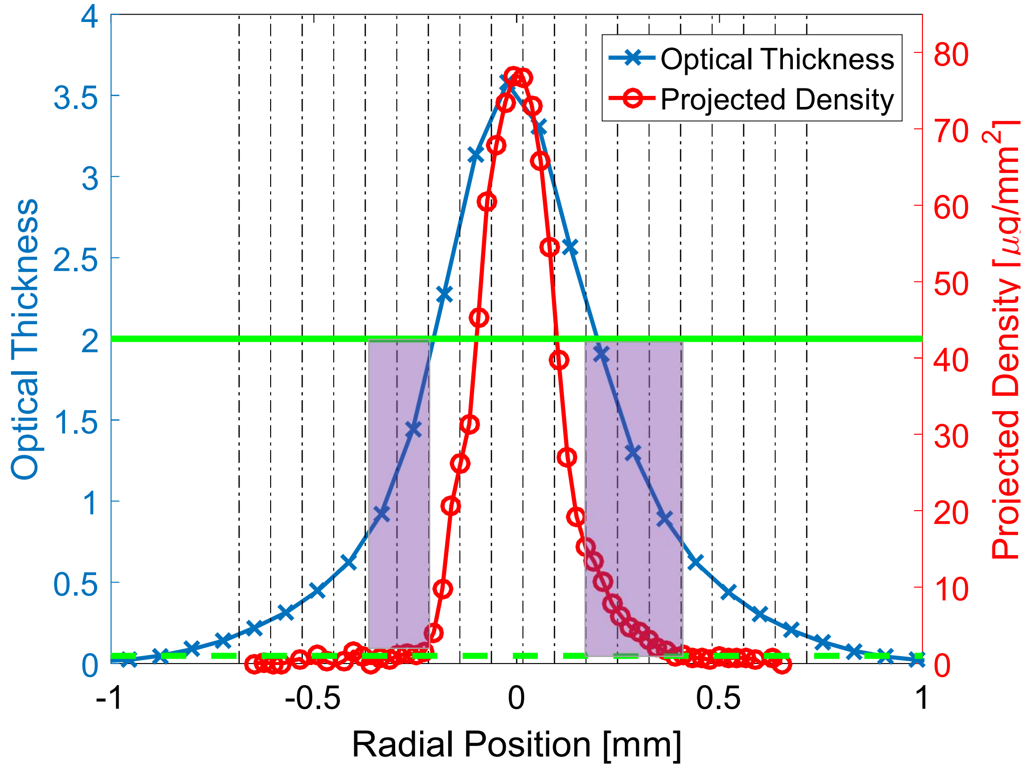

Figure 16: The optical thickness and projected density values for Spray D 2.4 kg/m3 50 MPa at an axial location of 10 mm.

Figure 16 shows another important processing step: identifying the regions where the SAMR measurement is valid without correction for the impact of multiple-scattering. As demonstrated in the theoretical development of the SAMR theory, the Mie-scatter calculations used to quantify SAMR SMDs are limited to single scattering. For Phase I, both conditions were met. In Figure 16, the purple shaded boxes indicate the regions where a measurement ratio could be taken. For Phase II and III of the project, a multiple scattering correction was employed which removed the $\tau < 2.0$ restriction on the utility of the SAMR technique. For these phases, the measurement ratio was only restricted to satisfying b).

Multiple scattering has a significant impact on a scattering-based measurement with a finite collection angle. To eliminate the restriction of a), the contribution of multiple-scattering must be accounted for. Therefore, the measured optical thickness must be corrected to achieve an accurate SMD estimation using the proposed method. Correcting for the multiple scattering effect will allow for a measurement ratio to be taken everywhere throughout the spray. This will provide a better understanding of the SMD field. To correct for multiple scattering, the modification proposed by Berrocal et al. is first adapted to the current optical system and then used to correct the measured optical thickness [14, 15].

According to Berrocal, the measured optical thickness (τ_{meas}) can be corrected (τ_{corr}) using the following equation which accounts for the influence of multiply scattered light [15]. This relation is for a measurement system with an infinitesimally small collection angle.

$$\tau_{meas} = \tau_{corr} - \alpha\, \tau_{corr}^{\beta} \tag{26}$$

where the coefficients α and β are related to the collection angle of the detection system and size of droplets present in the probe volume. Berrocal et al. reported the values of these coefficients for two collection angles of 3.3° and 10.3° (i.e. recalculated in a manner consistent with the current work) and mono-disperse particle sizes ranging from 1 to 20 μm, illuminated by a 800 nm light source [14, 15]. These constants are linearly interpolated to match the collection angle of the DBI experiments stated in Table 2. The difference in the wavelength of light source is also corrected. According to the theory of light scattering, particles of identical size parameter demonstrate the same scattering behavior [9]. The size parameter x is defined as

$$x = \frac{\pi d}{\lambda} \tag{27}$$

where d is the size of particles and λ is the wavelength of the incident light. Equation (19) is used to find the size of droplets exhibiting similar scattering behavior at 633 nm to those reported in the literature, d_{800}, illuminated at 800 nm [14, 15]

$$d_{633} = \frac{633}{800}\, d_{800} \tag{28}$$

Table 5 shows the diameters reported in the literature and those calculated to relate the 633-nm light source from the DBI experiments to the 800-nm light source used in the literature.

Table 5: Droplet sizes that produce the same effective scattering as an 800-nm light source.

d_{800}	d_{633}
1 μm	.79 μm
5 μm	3.9 μm
10 μm	7.9 μm

Equations (17) and (19) are then used to construct a transfer function which corrected the measured optical thickness using the current system, as seen in Figure 17. The measured optical thickness and local droplet size both must be known to do this. While the former is directly measured through the experiments, the latter is initially an unknown parameter. Therefore, an iterative process is required to solve Equation (17). The transfer function is coupled to Equation (17) and solved iteratively to compute the corrected optical thickness of the spray field and the corresponding SMD [4].

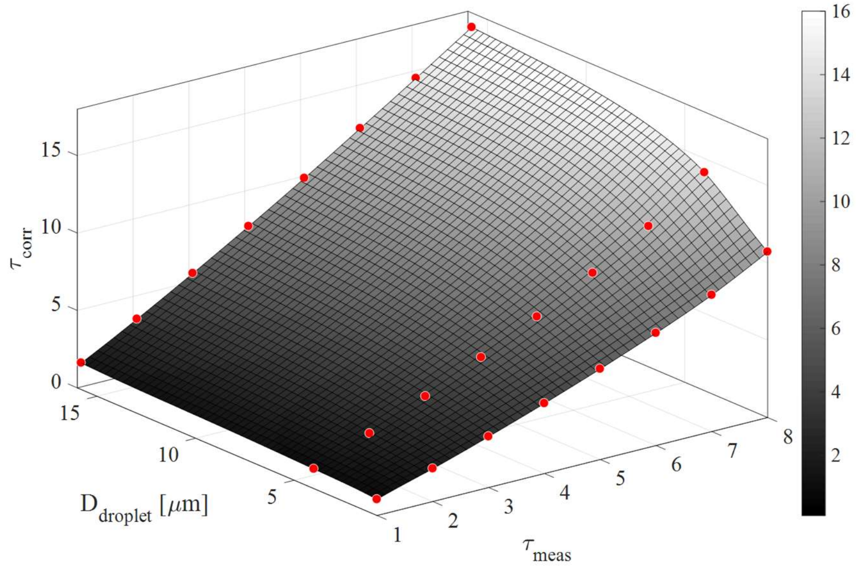

Figure 17: Graphical representation of the transfer function to correct the measured optical thickness for multiple scattering errors as a function of the local droplet size.

Figure 18 illustrates the contribution of multiple scattering on the measured optical thickness for the Spray A 22.8 kg/m^3 and 50 MPa 10 mm away from the nozzle exit. Multiple scattering has a significant impact on the DBI measurement at the spray centerline where the optical thickness is the highest [4]. It becomes less severe and eventually negligible towards the periphery of the spray, where the corresponding optical thickness approaches zero. This trend is expected largely due to the dominance of low-order scattering events in this region [4]. The multiple scattering correction was employed in the regions where this phenomenon may be of considerable impact (i.e. $\tau > 1$) for Phase II and III of this work.

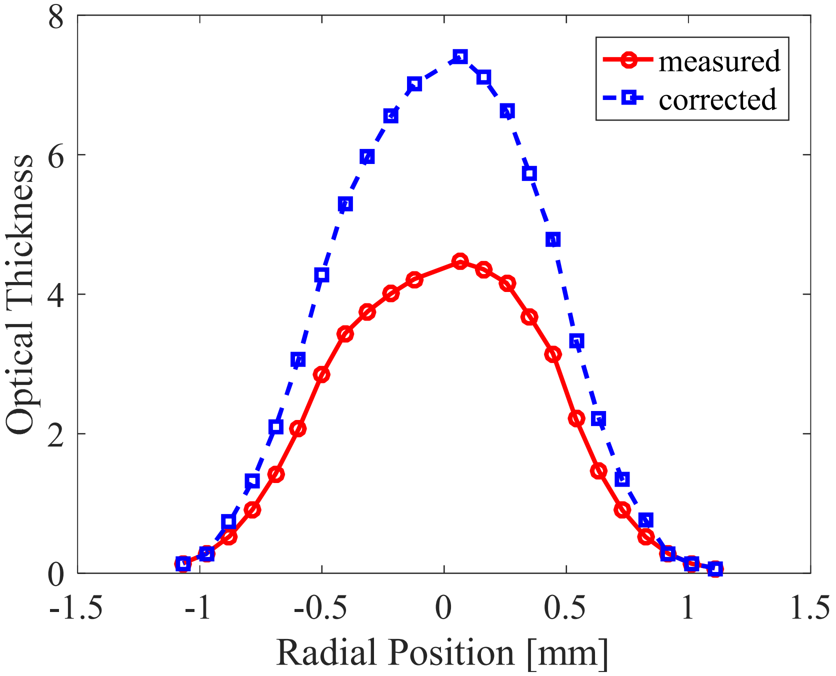

Figure 18: Measured and corrected optical thickness for Spray A 22.8 kg/m3 50 MPa at an axial location of 10 mm.

After identifying the regions where a measurement ratio could be conducted, the projected density values were curve fit. Curve fitting reduces the inherent noise present in experimental measurements and smooths the data. The curve fits were used to quantify the average projected density in each bin. The curve fitting technique varied for each data set. For the low back pressure cases, asymmetries are present in the spray. Therefore, it was necessary to employ separate curve fits for each condition. Some axial locations had features that could not be easily curve fit, such as the “shoulder” seen in the projected density data on the left-hand side of the spray as seen in Figure 19a. These asymmetries are seen at multiple axial locations for the 1.2 kg/m^3 ambient density condition and are therefore, not likely to be artifacts of noise. To capture these aspects of the spray, each axial location was individually curve fit. The curve fits had an R^2 value greater than 0.98. The curve fits accurately represented the trends in the data.

Figure 19a and b show the curve fits for the left and right half of the projected density distributions at the 10, 16 and 20-mm axial locations, respectively. For the left half of the spray (Figure 19a) for the 10 and 16 mm axial locations, two separate curve fits are used to capture the complex shape of the data, namely the “shoulder” in the projected density data. The data is broken up into two segments surrounding the “shoulder.” The first segment was fit with an exponential function of the form,

$$f(x) = Ae^{Bx} + Ce^{Dx} \tag{29}$$

where *A*, *B*, *C*, and *D* are unique fitting coefficients. For the 10mm axial location, the second segment of data points was fit with a three term polynomial function of the form,

$$f(x) = Fx^3 + Gx^2 + Hx + I \tag{30}$$

where *F*, *G*, *H*, and *I* are unique fitting coefficients. For the 16mm axial location, the second segment of data points was fit with an exponential function of the form,

$$f(x) = \mathrm{J}e^{\mathrm{K}x} + \mathrm{L}e^{\mathrm{M}x} \tag{31}$$

Where *J*, *K*, *L*, and *M* are unique fitting coefficients. The 20mm location was curve fit using a single Gaussian function,

$$f(x) = Ne^{-(\frac{x-P}{Q})^2} \tag{32}$$

For the right half of the spray (Figure 19b), the radial distribution was more uniform and could be easily fit with an exponential curve fit of the form of Equation (23). For phase I of the project,

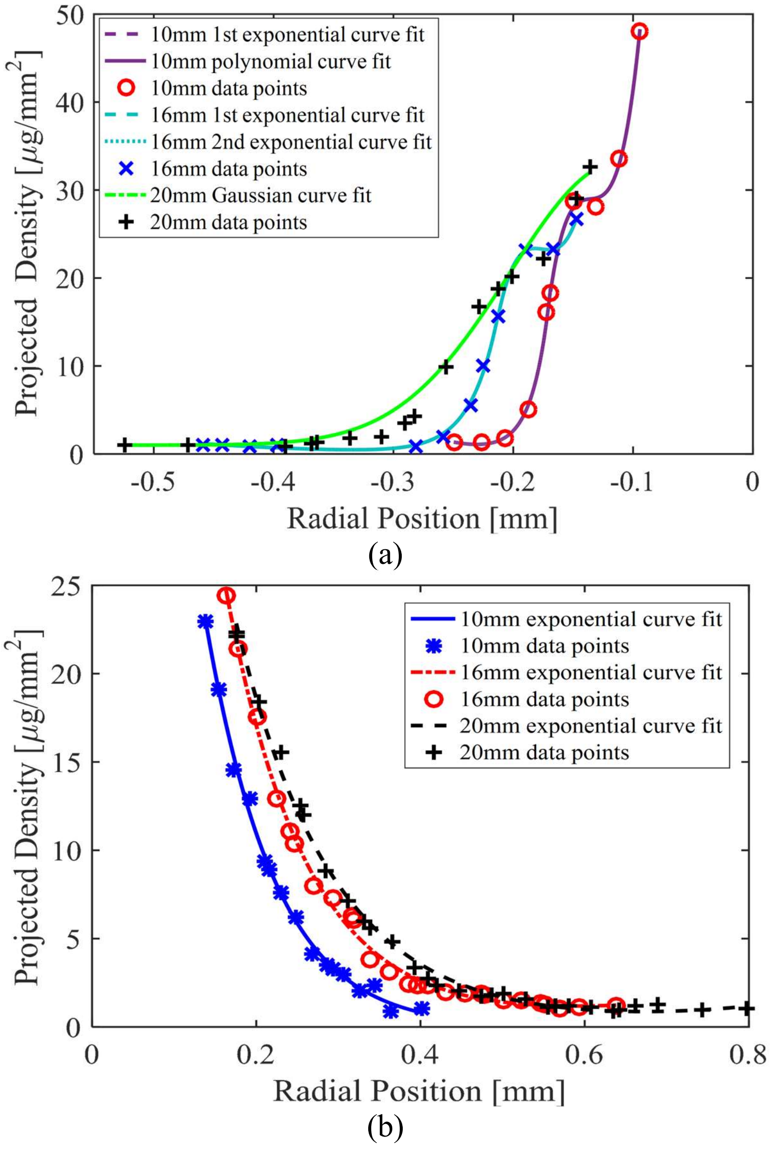

(a)

(b)

Figure 19: Projected density measurements and their respective curve fits for Spray D 1.2 kg/m3 50MPa three axial locations (10 mm, 16 mm, and 20 mm) for the left half (a) and right half (b) of the spray.

only the wings of the spray needed to be curve fit because these were the viable measurement regions. For phase II and III, the entirety of the spray was curve fit.

For higher back pressure cases, a Gaussian or double Gaussian curve fit was sufficient to accurately follow the trends and to smooth the data. In Phase III, the projected density from the 90, 120 and 150° viewing angles, show asymmetries that required careful curve fitting. A new curve fitting method was used to accurately capture the behavior of the data along the wings of the spray and near the spray centerline. A moving average was used to curve fit the radiography data along the wings and a Gaussian curve fit was used to curve fit the centerline data.

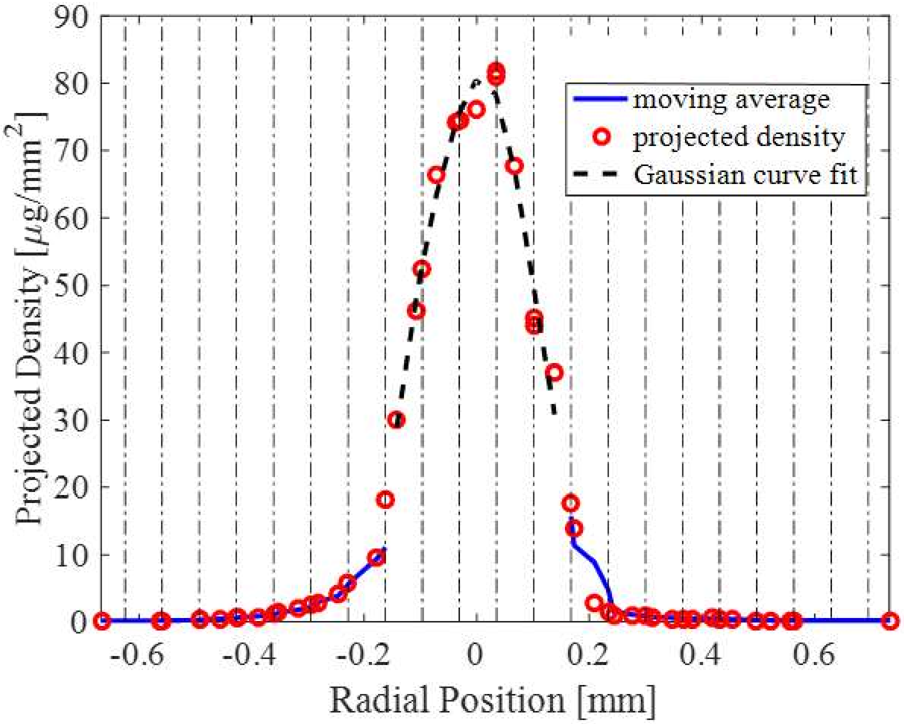

Figure 20: Curve fit of projected density values using a moving average along the wings and a Gaussian curve fit at the centerline for Spray D 1.2kg/m3 50MPa at 10 mm for 90° orientation.

Once a curve fit has been applied, the average under the curve for the projected density is calculated. After the average projected density value is calculated and overlaid with the optical thickness points (see Figure 20), the SAMR ratio is taken between the average projected density value divided by the fuel density and the optical thickness value. The measurement ratio is then related to C_{ext} from MiePlot as discussed previously and the SMD is calculated.

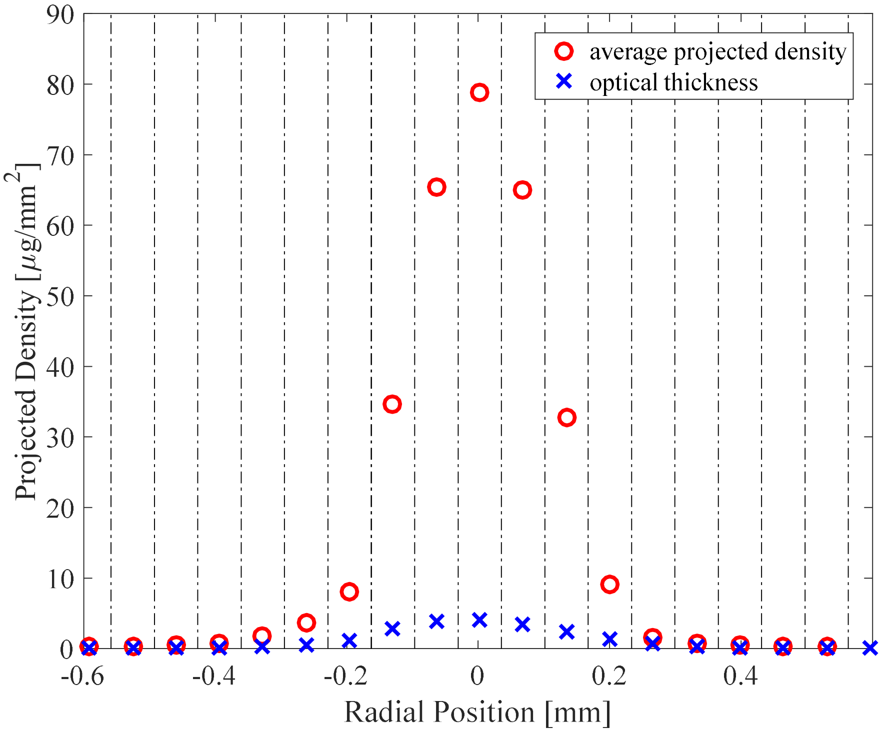

Figure 21: Average projected density values and optical thickness values for Phase III Spray D 1.2 kg/m3 50 MPa at 10 mm for 90° orientation.

5.1.3 Phase I SAMR Measurements of SMD in ECN Spray D

The primary goal of Phase I was to demonstrate and validate the SAMR diagnostic as a proof-of-concept. Figure 22-Figure 31 show radial distribution plots of SMD for multiple experimental conditions using the SAMR diagnostic. USAXS SMD results are overlaid on Figure 23-Figure 28 to validate the SAMR measurements.

Figure 22 indicates that a dense region of larger sized droplets exists closer to the spray centerline, with smaller sized droplets along the spray periphery. The right half of the spray also shows that the 16 mm and 20 mm axial locations have droplets similar in size. This suggests that a quasi-stable droplet size has been reached at these downstream locations. Also, the data demonstrates that there are asymmetries in the spray. As seen in Figure 22, the SMD measurements for the right half of the spray show a more gradual decrease in droplet size with increasing distance from the spray centerline than for the left half of the spray. The asymmetry of the radial distribution is likely to be strongly affected by the orientation of the diffuse-back illumination and x-ray radiography measurements. The asymmetry observed in the spray SMD distributions indicate that the assumption of a symmetric spray is not always valid, especially at this low backpressure conditions (1 bar). Figure 22 shows that asymmetries are evident in both the DBI and radiography measurement results, particularly evident in the “shoulder” seen in the left side of the projected density data. These spray features may stem from the machining groove that is present along the interior of the Spray D #209133 orifice [16].

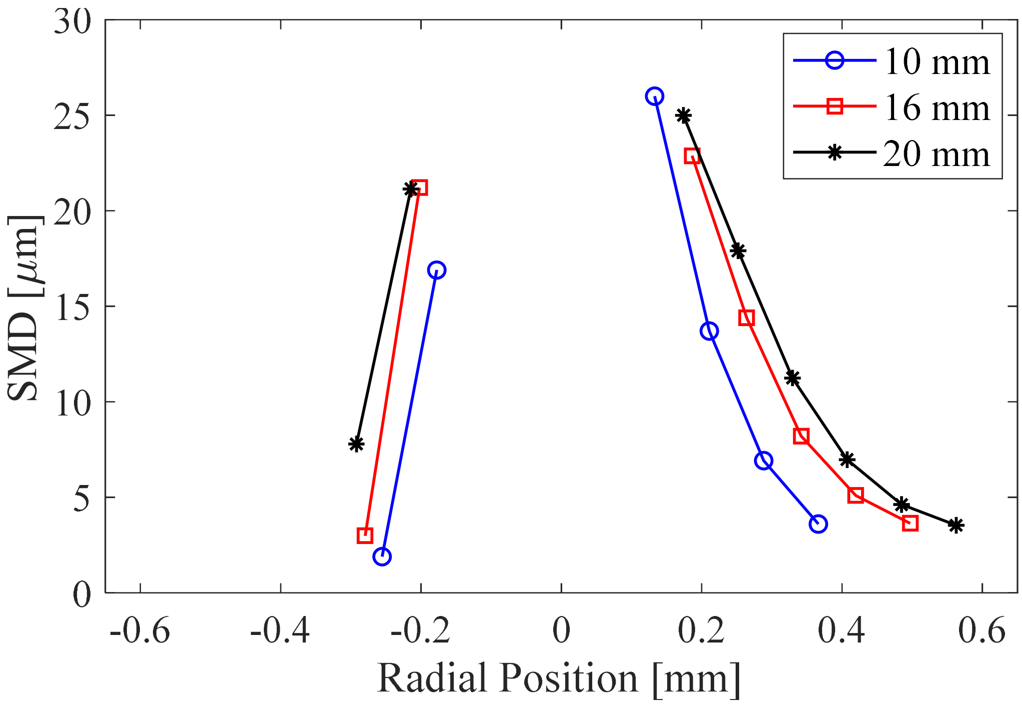

Figure 22: Phase I SAMR SMD results for Spray D 1.2 kg/m^3 500 bar at axial locations of 10, 16, 20 mm.

Figure 23 and Figure 24 show the Phase I SAMR SMD results validated against USAXS measurements conducted at Argonne National Lab for the Spray D injector at an ambient density of 1.2 kg/m^3 and injection pressures of 500 bar and 1500 bar, respectively. Larger droplets exist closer to the spray centerline. Moving away from the spray centerline produces droplets smaller in size. The Phase I results do not show droplet sizes at the spray centerline because the multiple scattering correction had not yet been developed and employed. For this data campaign, the SAMR measurement produces larger droplets than the USAXS measurement.

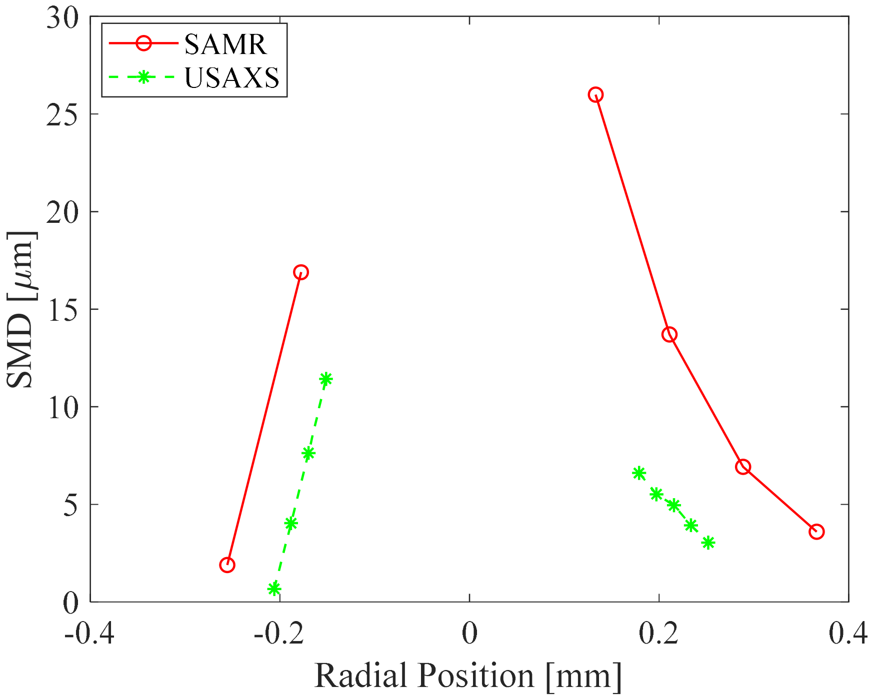

Figure 23: Phase I SAMR SMD results validated against USAXS measurements for Spray D 1.2 kg/m3 500 bar at an axial location of 10 mm.

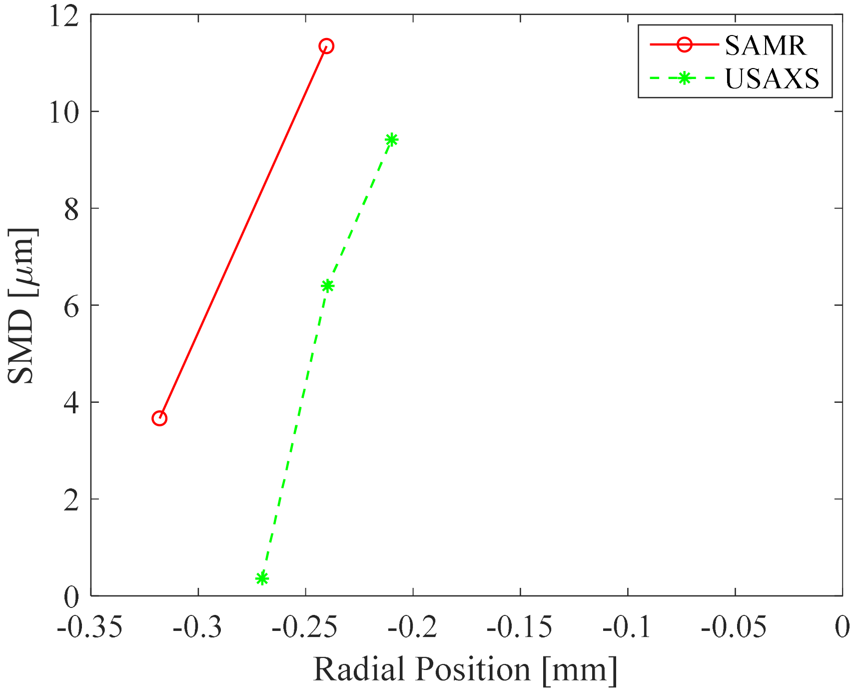

Figure 24: Phase I SAMR SMD results validated against USAXS measurements for Spray D 1.2kg/m3 1500 bar at an axial location of 10 mm.

Table 6: Percent difference between SAMR (Phase I) and USAXS for Spray D 1.2 kg/m3 500 bar for an axial location of 10 mm.

SAMR		USAXS		% Difference in SMD	% Difference in location
Radial Position (mm)	SMD (µm)	Radial Position (mm)	SMD (µm)		
0.13	26.0	0.18	6.6	119%	29%
0.21	13.7	0.20	5.5	85%	6%
0.29	6.9	0.25	3.0	78%	14%

Table 6 shows the percent difference in droplet size and location between the SMD results presented in Figure 23 for the USAXS and SAMR diagnostics. Near the spray center line, the difference in droplet size between USAXS and SAMR is about 19 µm. One reason for the large difference in droplet size could be that at these locations close to the center line, the optical thickness value approaches the threshold of $\tau = 2$ and thus the DBI measurement could be susceptible to errors associated with multiple scattering. As the radial distance from the centerline increases, the difference between the SAMR and USAXS SMDs decrease. At the furthest positive position, the difference in droplet size is only 3.8 µm. From Figure 23 and Figure 24, it appears that there is some misalignment between the USAXS and SAMR results. It looks like the data may be shifted radially from each other, suggesting that the data are not truly co-aligned. Another source of uncertainty with this USAXS campaign is improper alignment of the surface area and the radiography measurements. When the USAXS transverse scan is performed, the beam is centered at the peak value of maximum signal intensity, which should theoretically align with the spray centerline [7]. Unfortunately, this cannot be confirmed since Argonne researchers are unable to take the radiography and USAXS measurement simultaneously.

To reduce the measurement uncertainty in the USAXS data, researchers at Argonne completed another campaign which focused on obtaining a greater number of radial measurements of SMD and ensuring proper alignment of the measurement injector and viewing angle between experiments at GA Tech and Argonne. Figure 25-Figure 28 show the comparison of SMD results for the SAMR and USAXS techniques. These updated USAXS results and SAMR results show good agreement in droplet size. Some uncertainty remains in proper co-alignment between the SAMR and USAXS methods. Currently, the USAXS data is shifted via FWHM prior to overlaying it with the SAMR results. The right half of the spray (positive half) is mostly presented here because more viable data locations for the SAMR were present at these regions. Figure 25 shows larger sized droplets near the spray centerline. The droplets decrease in size as the radial position is increased. The SMDs show decent agreement with the maximum difference in droplet size being about 3.9 µm.

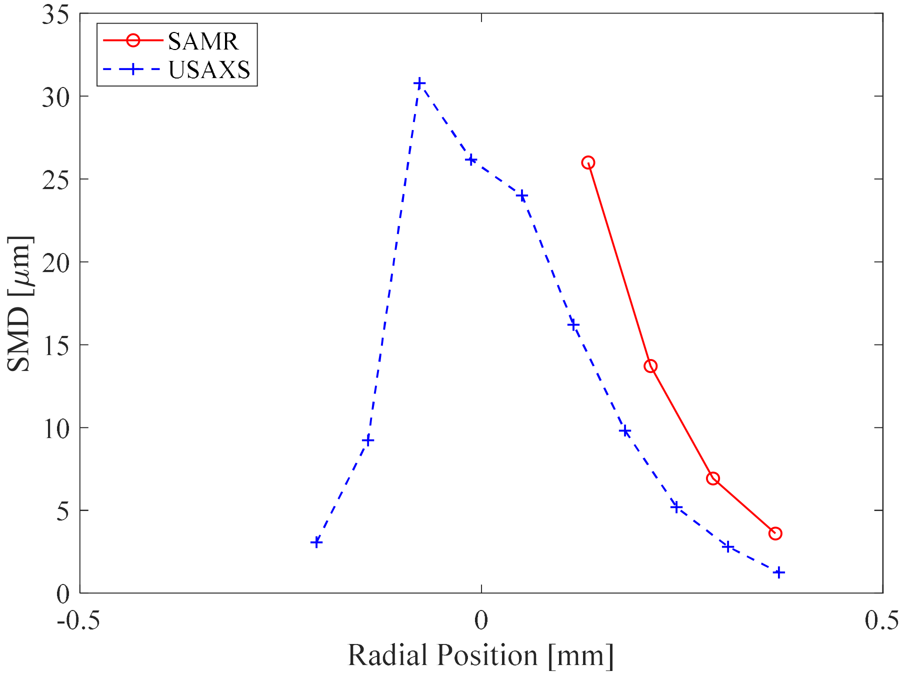

Figure 25: Phase I SAMR SMD results validated against USAXS measurements for Spray D 1.2 kg/m3 500 bar at an axial location of 10 mm.

Table 7: Percent difference between SAMR (Phase I) and USAXS for condition presented in Figure 25.

SAMR		USAXS		% Difference in SMD	% Difference in location
Radial Position (mm)	SMD (μm)	Radial Position (mm)	SMD (μm)		
0.13	26.0	0.05	24.0	8%	89%
0.21	13.7	0.18	9.8	33%	16%
0.29	6.9	0.24	5.2	28%	17%
0.37	3.6	0.31	2.8	25%	18%

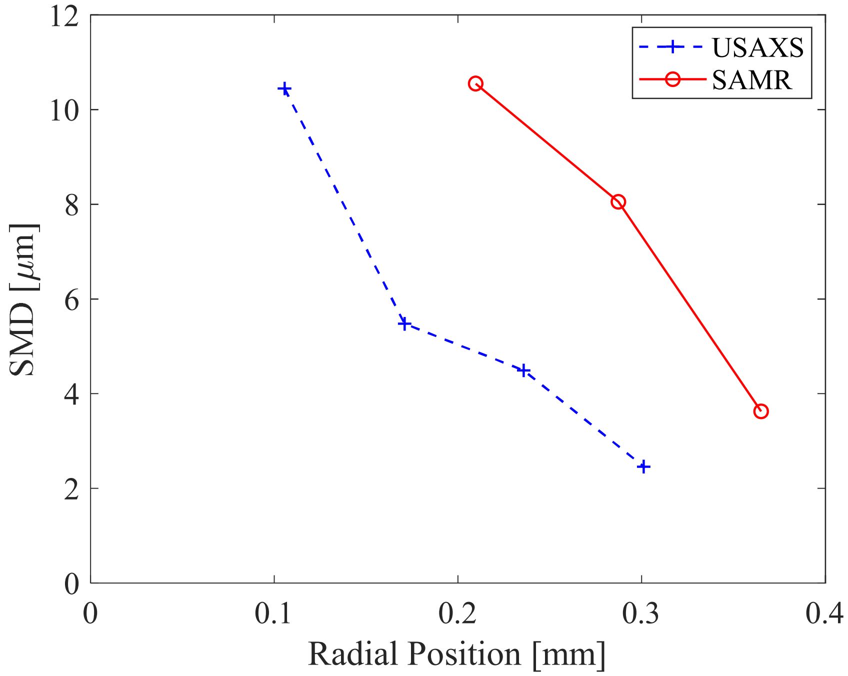

Figure 26: Phase I SAMR SMD results validated against USAXS measurements for Spray D 2.4 kg/m3 500 bar for an axial location of 10 mm.

Table 8: Percent difference between SAMR (Phase I) and USAXS for condition presented in Figure **26**.

SAMR		USAXS		% Difference in SMD	% Difference in location
Radial Position (mm)	SMD (µm)	Radial Position (mm)	SMD (µm)		
0.21	10.6	0.11	10.4	1%	66%
0.29	8.1	0.17	5.5	38%	51%
0.36	3.6	0.30	2.5	38%	19%

Table 9: Percent difference between SAMR (Phase I) and USAXS (Cycle2017_3) for condition presented in Figure **27**.

SAMR		USAXS		% Difference in SMD	% Difference in location
Radial Position (mm)	SMD (µm)	Radial Position (mm)	SMD (µm)		
0.32	6.8	0.14	7.3	7%	77%
0.40	5.4	0.19	4.0	29%	69%
0.48	4.6	0.29	3.2	38%	46%
0.55	3.7	0.35	2.1	53%	45%

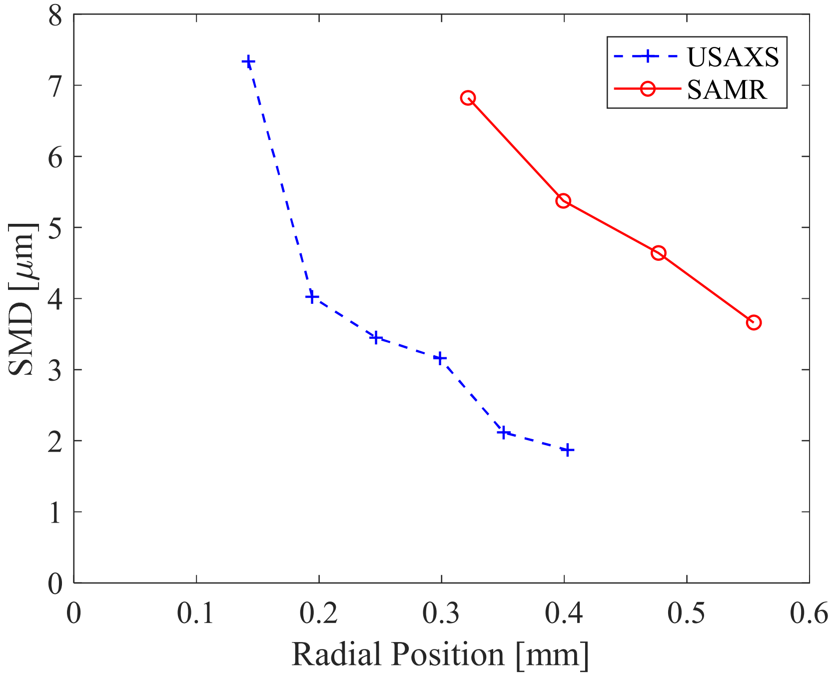

Figure 27: Phase I SAMR SMD results validated against USAXS measurements for Spray D 2.4 kg/m3 500 bar for an axial location of 15 mm.

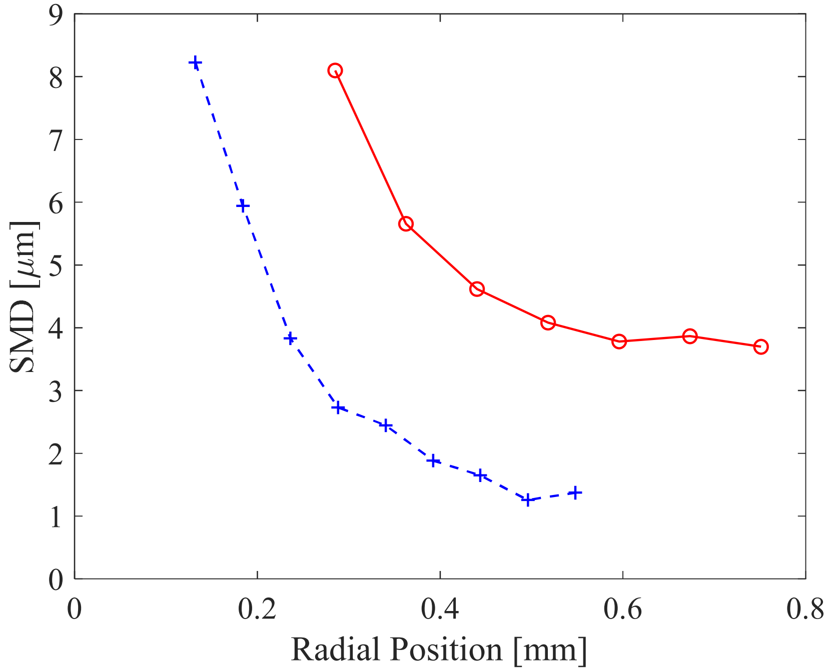

Figure 28: Phase I SAMR SMD results validated against USAXS measurements for Spray D 2.4 kg/m3 500 bar for an axial location of 20 mm.

Table 10: Percent difference between SAMR (Phase I) and USAXS (Cycle2017_3) for condition presented in Figure **28**.

SAMR		USAXS		% Difference in SMD	% Difference in location
Radial Position (mm)	SMD (µm)	Radial Position (mm)	SMD (µm)		
0.28	8.1	0.13	8.2	2%	73%
0.36	5.6	0.18	5.9	5%	65%
0.44	4.6	0.23	3.8	19%	60%
0.52	4.1	0.34	2.5	50%	41%
0.59	3.8	0.39	1.9	67%	41%
0.67	3.9	0.44	1.6	80%	41%
0.75	3.7	0.55	1.4	31%	92%

Figure 26-Figure 28 show similar trends as before, decreasing droplet size as radial position increases. Table 8-Table 10 show the radial locations, SMD values, and corresponding percent differences for SAMR and USAXS measurements. While radial distributions of SMD at distinct axial positions are useful, two-dimensional color maps with interpolation provide a more complete picture of the spatial droplet evolution. These SMD maps are shown in Figure 29.

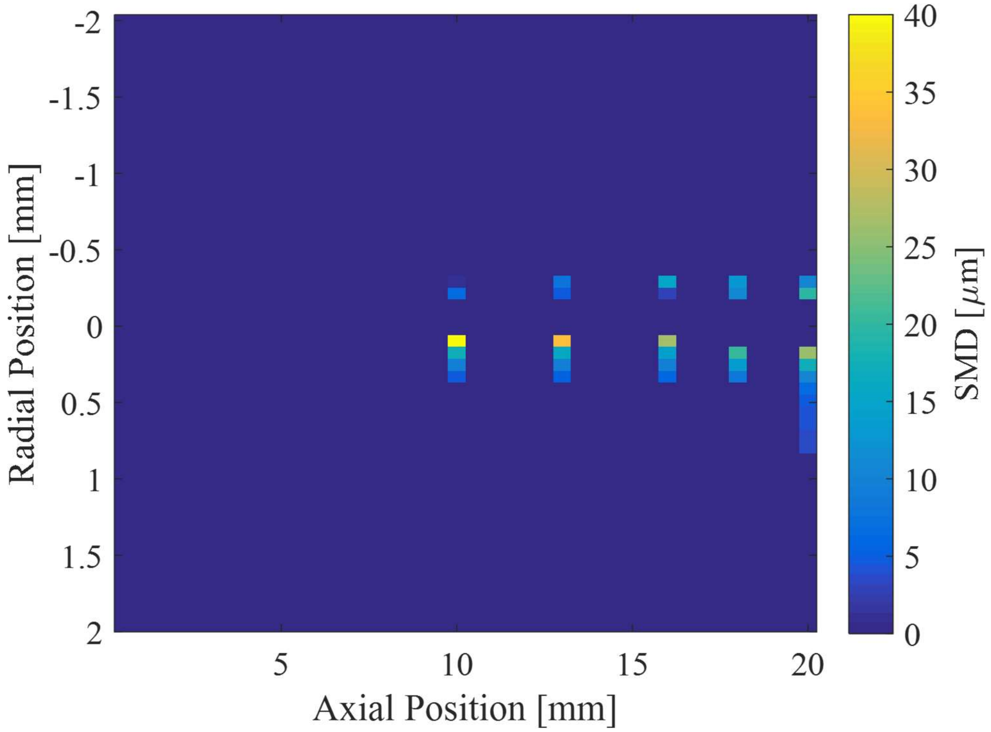

Figure 29: Phase I SMD map for Spray D 1.2kg/m3 50MPa with interpolated points at 13 and 18-mm axial positions.

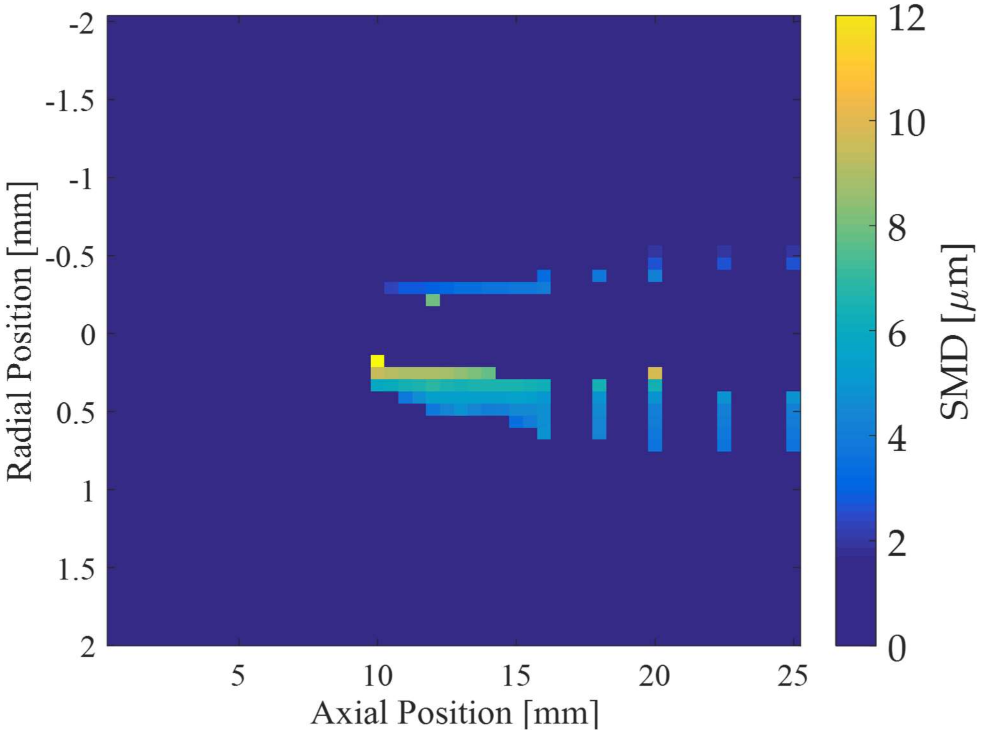

Figure 30: Phase I SMD map for Spray D 2.4 kg/m3 50 MPa with interpolated points at 10.5, 11.5, 12.5, 13.5, 14.5, 15.5, 18, 22.5-mm axial positions.

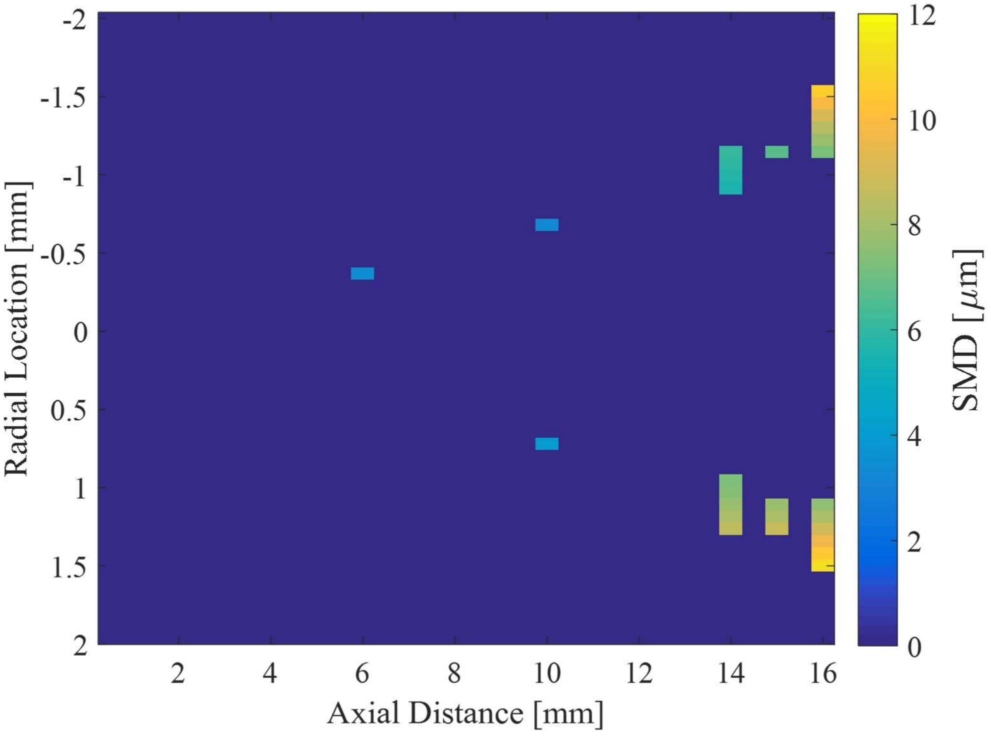

Figure 31: Phase I SMD map for Spray D 22.8kg/m3 50MPa with interpolated points at 15-mm axial position.

Figure 29 and Figure 30 show similar trends, larger droplets exist closer to the spray centerline, whereas smaller droplets occur along the spray periphery. Increasing axial distance from the nozzle exit results in smaller droplets. This trend is evident for the low ambient density cases (1.2 and 2.8 kg/m^3). As ambient density increases, this trend is not observed. For the 22.8 kg/m^3 ambient density case, at downstream axial locations, droplets increase in size as radial position increases, as seen in Figure 31. This counterintuitive trend has been observed by other researchers [17, 18, 19, 20, 21]. This increase in SMD at the spray periphery is primarily attributed to two potential mechanisms: droplet collision/coalescence at the peripheral region due to shear effects [20], and transport of large droplets from the core region due to vortex effects at the spray tip [21].

5.1.4 Phase II SAMR Measurements of SMD in ECN Spray A

Phase II SMD results are shown for Spray A at 22.8 kg/m^3 ambient density and 50 MPa injection pressure (Martinez, et al., 2018). Phase II DBI experiments improved the SAMR diagnostic by utilizing a single wavelength 633 nm red LED as the light source. Using a longer wavelength helps to suppress multiple scattering thus improving the fidelity of the optical thickness measurement in the intermediate scattering regime ($1 < \tau < 2$). Additionally, Phase II employed the multiple scattering correction, so the SMDs were calculated through the entire radial profile of the spray.

Figure 32 shows the radial distribution of SMDs using the measured and corrected optical thickness values. At the periphery of the spray where $\tau < 1$ and single scattering events are safely assumed, the multiple scattering correction was not applied, so the SMDs for the original and corrected values overlap. An average SMD of 6 μm is measured along the spray centerline. While the distribution of SMD remains fairly uniform for a large proportion of the spray width, it sharply rises at the peripheral region of the spray. This is particularly evident farther downstream of the injector at 16-mm axial location. As stated earlier, this counterintuitive trend has been witnessed by other researchers and can be attributed to droplet collision and coalescence due to shear effects and the transport of large droplets from the core region at the spray tip (Martinez, et al., 2018; Wu, Reitz, & Bracco, 1986; Kosaka, Suzuki, & Kamimoto, 1995).

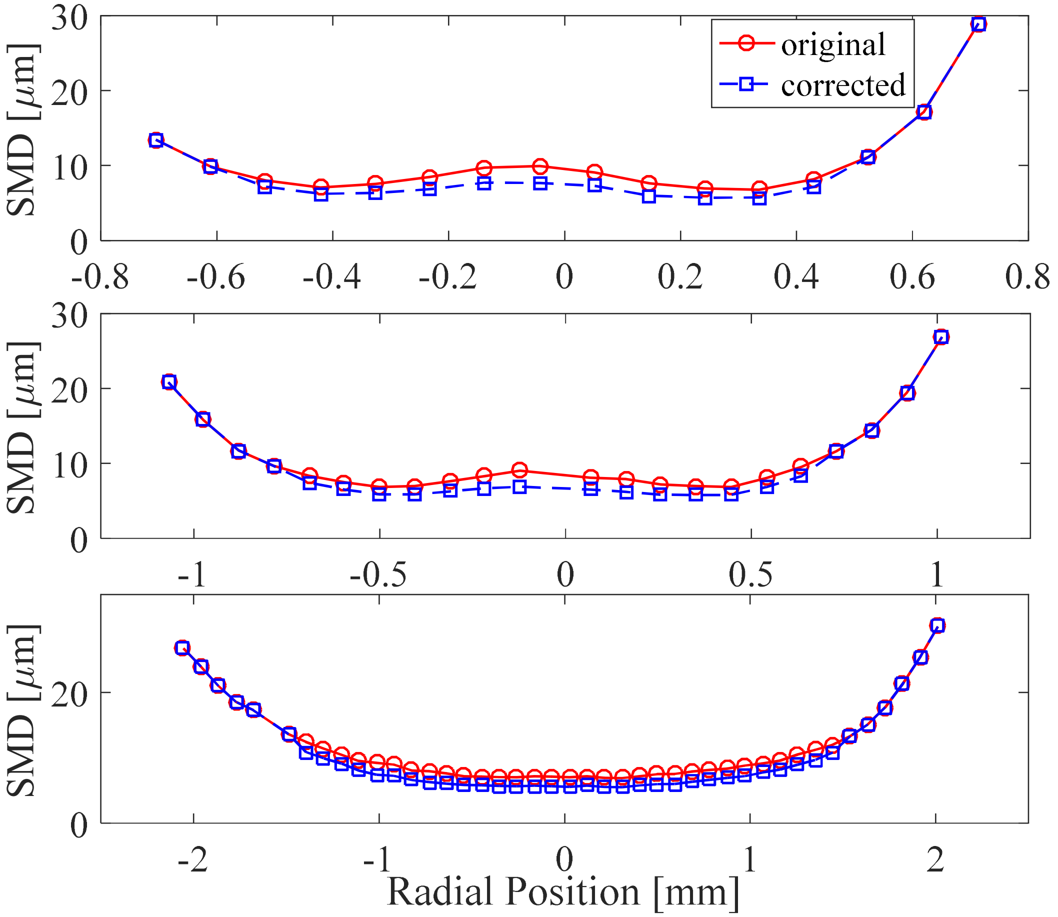

Figure 32: Radial distribution of measured and scattering-corrected SMDs for Spray A 22.8 kg/m3 50 MPa at 8-mm (top), 10-mm (middle), 16-mm (bottom) axial positions.

Figure 33 shows a detailed view at the regions where the multiple scattering correction was applied. In these regions, the uncorrected results overestimate the size of droplets by a maximum of about 2 µm. This is attributed to the contribution of multiple scattering phenomenon, which results in an underestimation of the local optical thickness (as shown in Figure 18) and hence an overestimation of the corresponding droplet sizes.

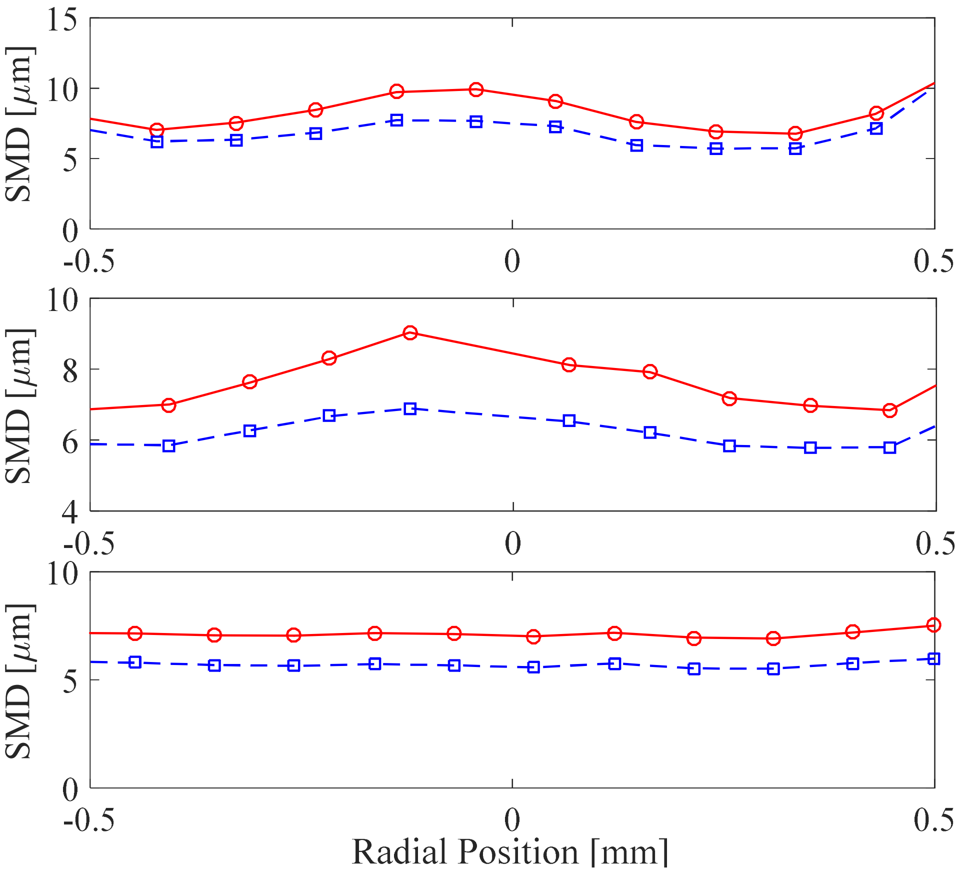

Figure 33: Detailed view of measured SMDs for Spray A 22.8kg/m3 50MPa at axial locations of 8 (top), 10 (middle), 16-mm (bottom) axial positions.

5.1.5 Phase III SAMR Measurements of SMD in ECN Spray D

Phase III used an optimized diagnostic setup for both diffuse back illumination and x-ray radiography for the SAMR technique to measure spray droplet sizes. The DBI setup used an ideal diffuse and uniform background and the maximum dynamic range of the camera. The finite collection angle is decreased, and a finer measurement resolution is achieved. A smaller collection angle reduces the light that is redirected into the detection system and thus reduces the errors associated with multiple scattering. A finer measurement resolution is beneficial because it provides more locations where the measurement ratio can be conducted. The radiography measurements increased the signal to noise ratio (SNR) by adding Cerium to the fuel and by increasing the number of fuel injections that were ensemble averaged. Increasing the SNR provides additional regions where the measurement ratio could be conducted. In phase III the data was taken at 3 injector orientations, which allows for analysis of the asymmetries present in the spray. Figure 34 shows an example of the original and corrected SMDs for the Spray D 1.2 kg/m^3 density at 50 MPa injection pressure and a 90° viewing angle. Without the multiple scattering correction, the measurement indicates that the droplets can reach up to 40 µm at the spray centerline. This is very large and has not been seen in the literature. The multiple scattering correction brings the SMDs at the centerline down to 20 µm, which is similar to results in the literature [22]. The droplets decrease in size traversing across the spray.

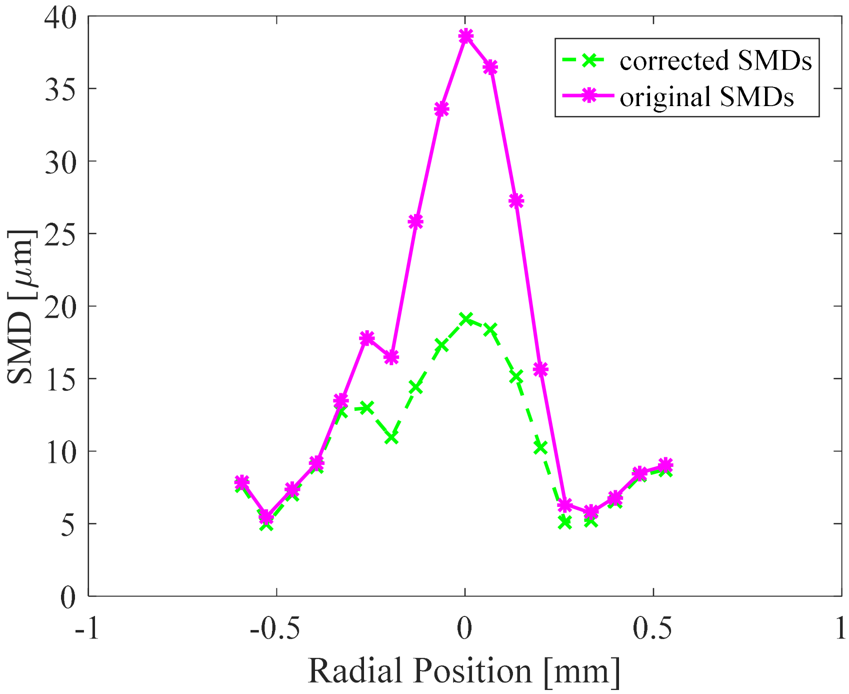

Figure 34: Comparison of as-measured and scattering-corrected SMDs for Spray D at 90° orientation and 10-mm axial location. $\rho_{amb} = 1.2$ kg/m^3, $P_{inj} = 50$ MPa.

Figure 35a-c shows the Phase III SMD results at 1.2 kg/m^3 50 MPa at 90°, 120°, and 165° orientations for axial locations at 10, 16, 20 mm. Each of the plots shows the same general trends. Larger droplets exist at the spray centerline, and they decrease in size as radial position increases. Additionally, increasing axial distance results in decreasing droplet size. Besides these two trends, Figure 35 clearly shows the asymmetries present in the spray. If the spray was perfectly symmetric, the radial distributions of droplet size would overlap, but this is not evident in the figures. Figure 35a) shows a particularly interesting trend; the 90° orientation shows a much smaller droplet size throughout the spray compared to the 120° and 165° orientations. At the centerline, the difference in SMD between the 90° and 120° is 11.4 µm. The 165° orientation shows a bimodal distribution, as evident by the double peak of 24.6 µm and 27.6 µm at -.10 mm and .09 mm, respectively. At the 16 mm axial location (seen in Figure 35b), the droplet size radial distribution of the 120° and 165° orientations converge at the spray periphery (-.34 to -.19 mm) and (.19 to .32 mm). The 165° orientation at 16 mm also shows the bimodal distribution, with both SMD peaks hovering around 19 µm at -.14 mm and .06 mm. At the 20 mm axial location (Figure 35c), the 120° and 165° orientations converge even more. The peak/centerline SMDs also converge for 90°, 120°, and 165° orientations.

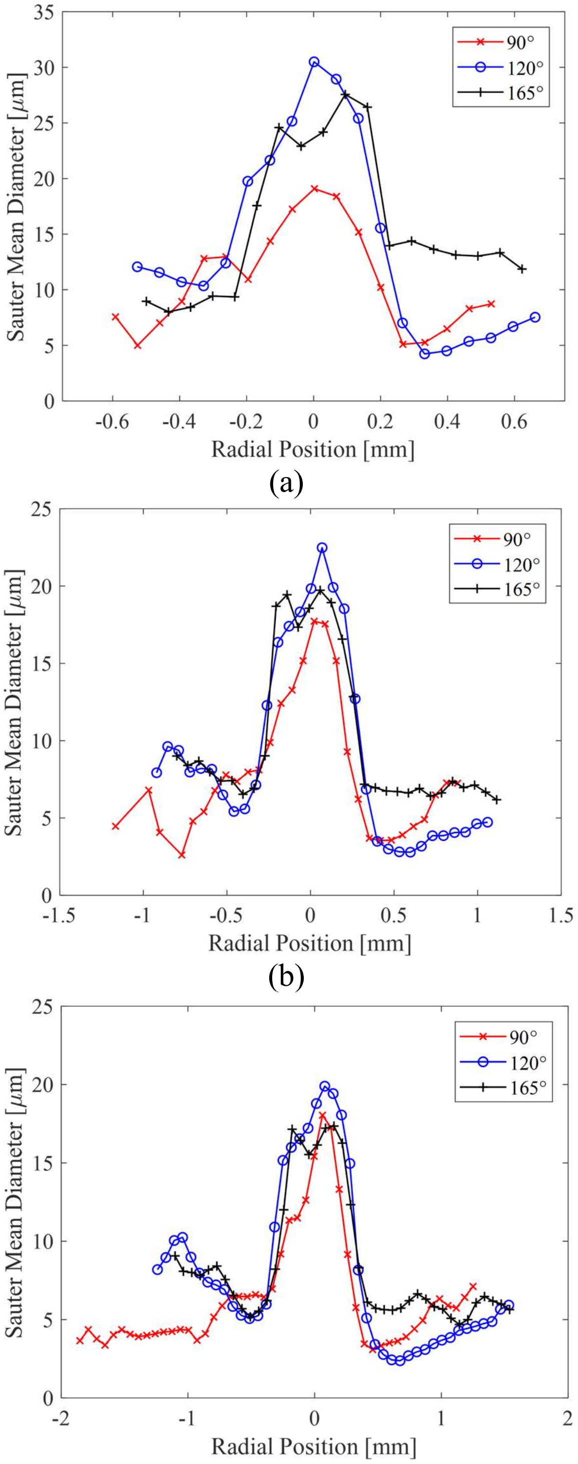

Figure 35: Measured SMDs in Spray D at various injector orientations and at 10-mm (a), 16-mm (b), and 20-mm (c) axial locations. ρ_{amb} = 1.2 kg/m^3, P_{inj} = 50 MPa.

Table 11: Peak SMD measured along each radial spray profile in Figure 35a-c.

	10 mm	**16 mm**	**20 mm**
90°	19.1 µm	17.7 µm	18.0 µm
120°	30.5 µm	22.5 µm	19.9 µm
165°	27.6 µm	19.7 µm	17.4 µm

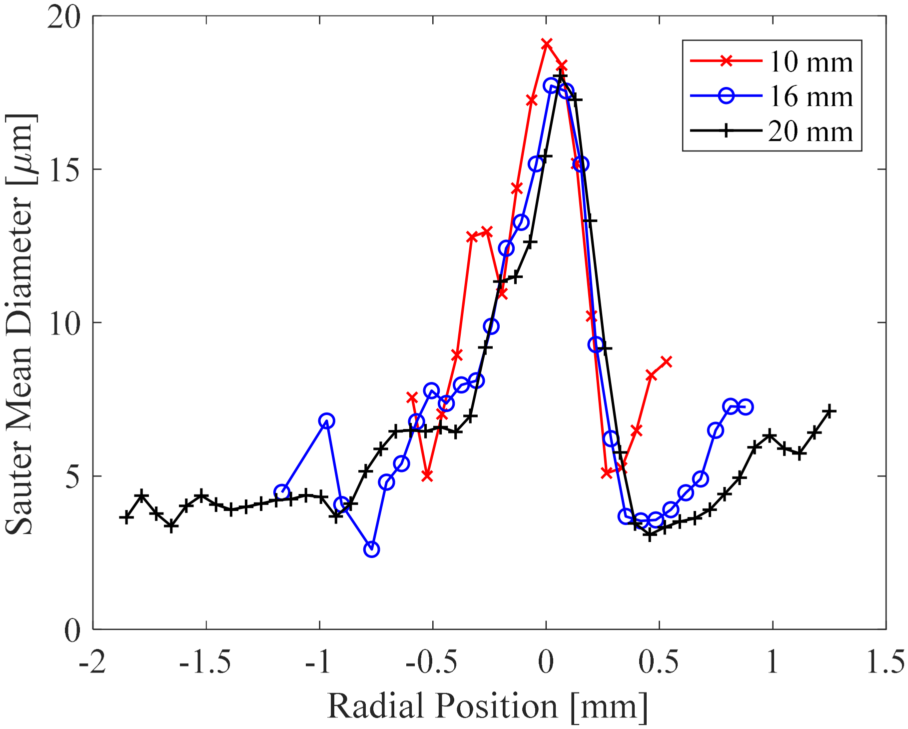

Figure 36: Measured SMDs in Spray D at various axial locations at a fixed injector orientation of 90°. ρ_{amb} = 1.2 kg/m^3, P_{inj} = 50 MPa.

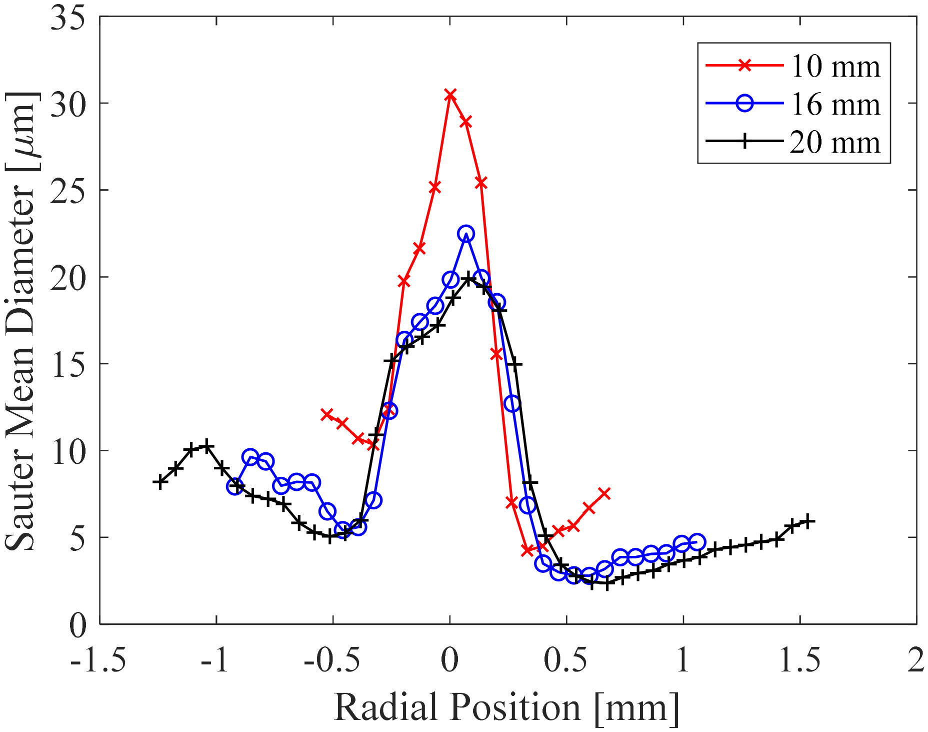

Figure 37: Measured SMDs in Spray D at various axial locations at a fixed injector orientation of 120°. $\rho_{amb} = 1.2$ kg/m^3, $P_{inj} = 50$ MPa.

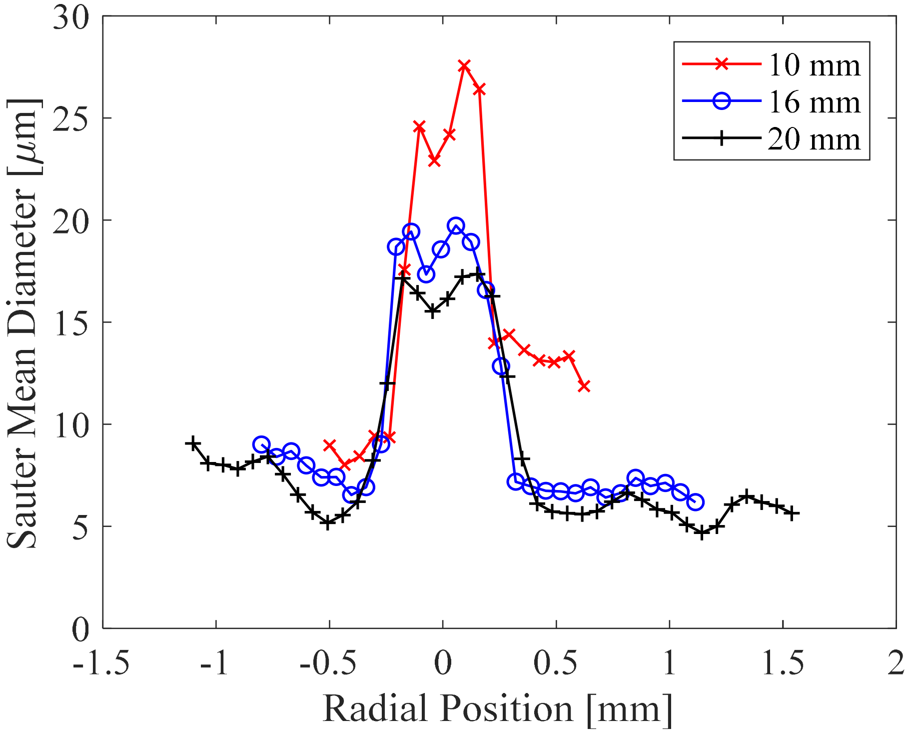

Figure 38: Measured SMDs in Spray D at various axial locations at a fixed injector orientation of 165°. $\rho_{amb} = 1.2$ kg/m^3, $P_{inj} = 50$ MPa.

Figure 36-Figure 38 show the SAMR SMDs for Spray D 1.2 kg/m^3 50 MPa at each orientation with all the axial positions overlaid. Figure 36 shows the SMDs for the 90° orientation. This plot illustrates all three axial locations overlapping near the spray centerline, with the peak SMD value decreasing slightly with axial distance. At 10 mm, the peak SMD is 19 µm. At 16 and 20 mm, the SMD hovers around 17.5-18 µm. As the radial position increases (from 0 to ±.5 mm), the SMD value decreases. From 0 to ±.5 mm, the SMDs overlap for 16 and 20-mm locations, indicating that a stable droplet size has been reached. However, for all three axial conditions, on the positive half of the spray from .5 to 1 mm, the SMD begins to increase. This interesting trend could be attributed to droplet collision and coalescence. The negative side of the spray also shows an interesting trend at the 10mm location, where a shoulder is seen around -.3 mm with an SMD value of 12.8 µm. Figure 37 and Figure 38 show the SMDs for the 120 and 165°, respectively. Both figures show similar trends. The 10 mm axial location shows a significantly larger droplet size than the 16 and-20 mm locations throughout the entirety of the spray. This is consistent with Phase I trends and many sources in the literature. Larger droplets exist closer to the nozzle, and they decrease in size as the distance from the nozzle increases. Figure 37 shows that at the 120° a singular SMD peak value occurs at the spray centerline, whereas Figure 38 shows that for the 165° orientation a double peak in SMD is seen. Both peak SMDs are centered around the spray centerline. The peak SMDs at 10 mm are 27.6 µm and 24.6 µm; at 16 mm the peak SMDs are 19.7 µm and 19.4 µm; at 20 mm the peak SMDs are 17.4 µm and 17.2 µm. It is quite curious that at this injector orientation, this bimodal distribution is very evident.

Figure 39-Figure 41 show two-dimensional SMD droplet sizing maps of this same data. These maps provide a better way to visualize the droplet evolution in space. These droplet sizing maps show that, as expected, the droplets decrease in size with increasing axial and radial position. The SAMR technique is demonstrated to yield a reasonable measurement of diesel spray droplet sizes, with the expected range of SMD reported in prior literature and following the expected trends in spatial evolution.

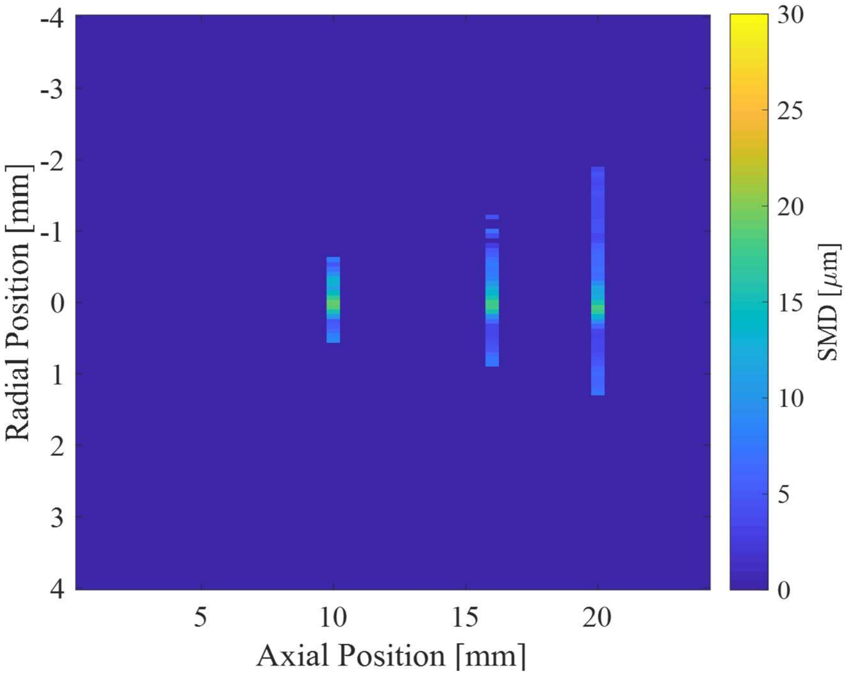

Figure 39: Map of measured SMDs for Spray D at a fixed injector orientation of 90°. $\rho_{amb} = 1.2$ kg/m^3, $P_{inj} = 50$ MPa.

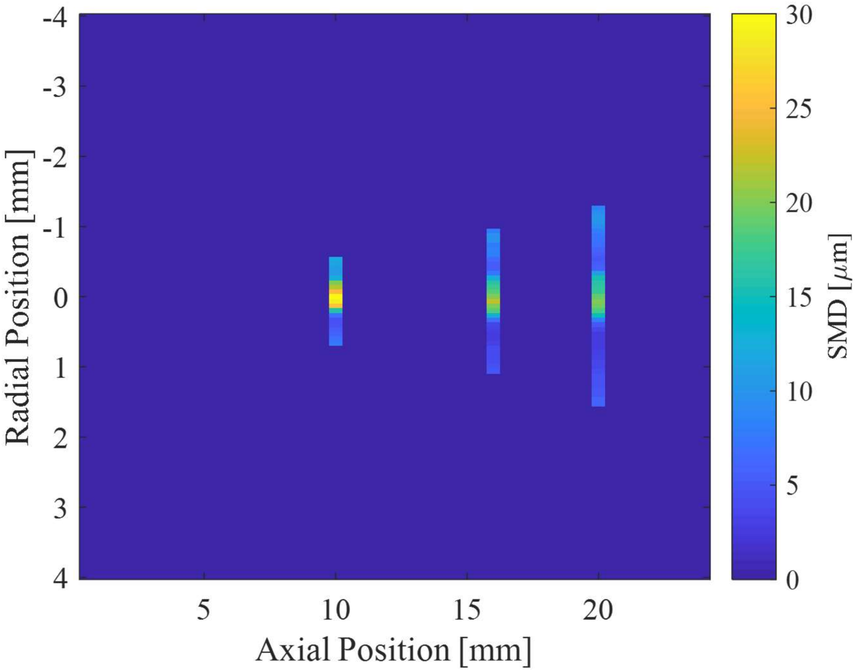

Figure 40: Map of measured SMDs for Spray D at a fixed injector orientation of 120°. $\rho_{amb} = 1.2$ kg/m^3, $P_{inj} = 50$ MPa.

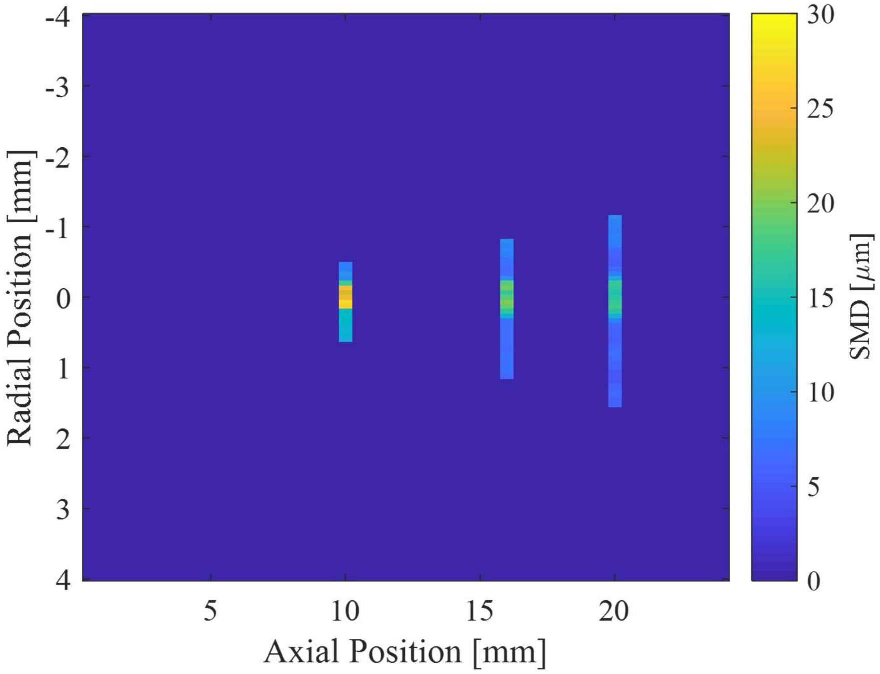

Figure 41: Map of measured SMDs for Spray D at a fixed injector orientation of 165°. ρ_{amb} = 1.2 kg/m^3, P_{inj} = 50 MPa.

Figure 42-Figure 44 show two-dimensional Sauter Mean Diameter plots which have been interpolated along the axial dimension from 10 to 20 mm using the MATLAB built in "scatteredInterpolant" function. These plots are expected to be particularly useful for model validation efforts where visualization of interpolated scalars is typical. All the figures have the color bar limits from 0 to 30 µm which enables a comparison of the injector orientations. The 90° orientation shows much smaller droplets than the 120° and 165° orientations, as seen previously. The figures also show the general trend that larger droplets exist near the spray centerline and they decrease in size as axial distance increases. Additionally, the droplets decrease in size as radial distance increases, until they reach a certain radial position where the droplet size begins to increase slightly.

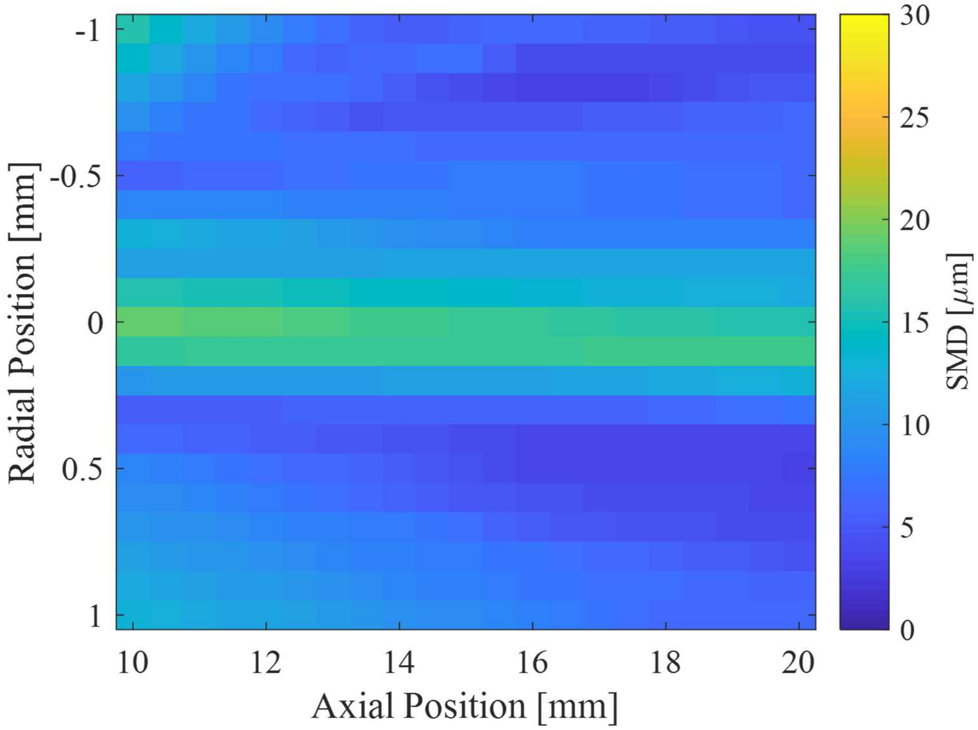

Figure 42: Interpolated map of measured SMDs for Spray D at a fixed injector orientation of 90°. $\rho_{amb} = 1.2$ kg/m^3, $P_{inj} = 50$ MPa.

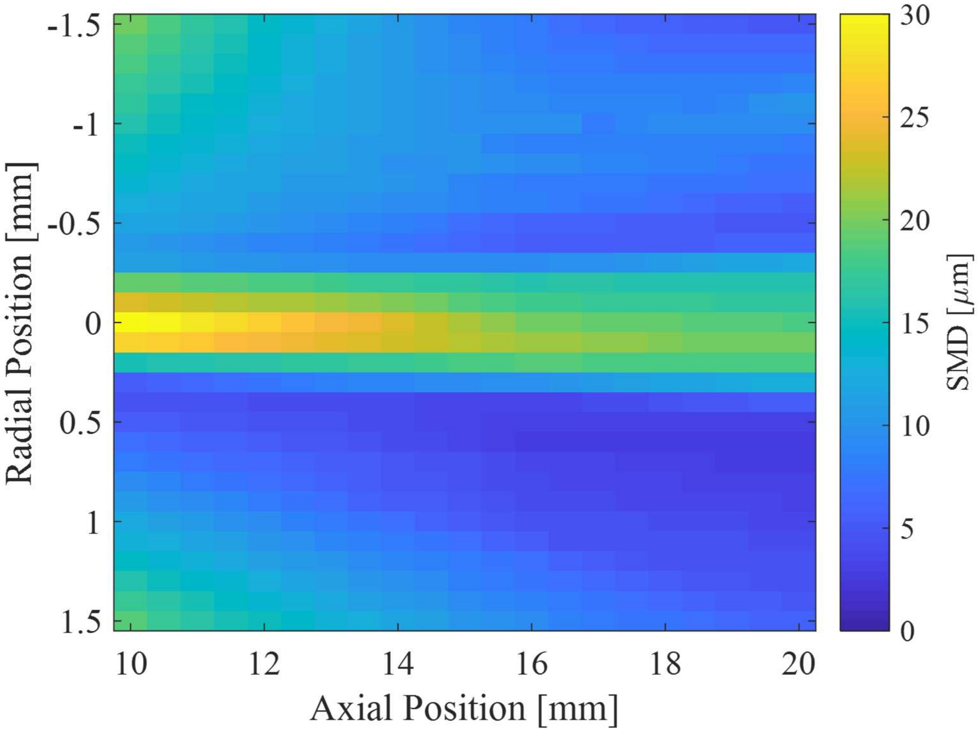

Figure 43: Interpolated map of measured SMDs for Spray D at a fixed injector orientation of 120°. $\rho_{amb} = 1.2$ kg/m^3, $P_{inj} = 50$ MPa.

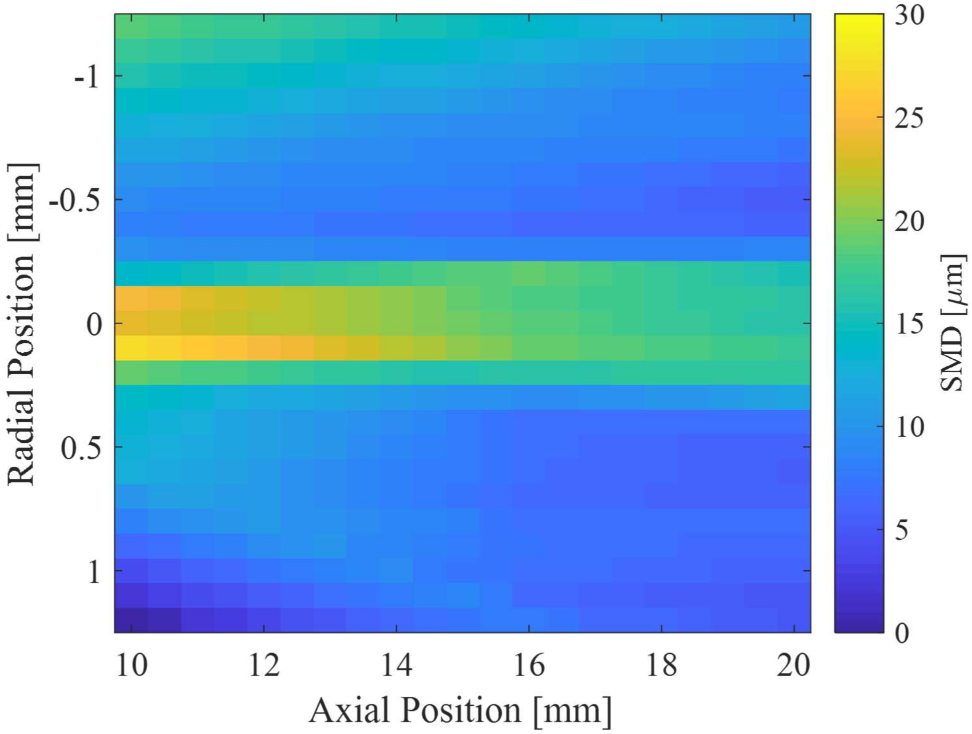

Figure 44: Interpolated map of measured SMDs for Spray D at a fixed injector orientation of 165°. ρ_{amb} = 1.2 kg/m^3, P_{inj} = 50 MPa.

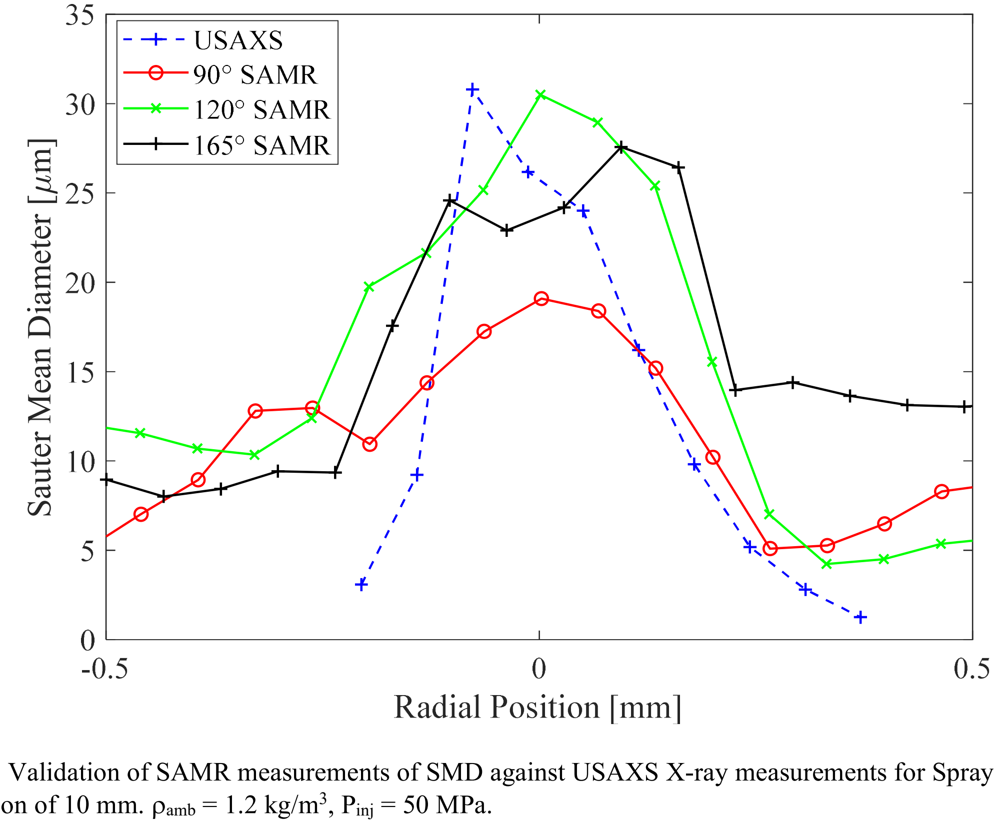

Figure 45: Validation of SAMR measurements of SMD against USAXS X-ray measurements for Spray D at an axial location of 10 mm. ρ_{amb} = 1.2 kg/m^3, P_{inj} = 50 MPa.

Table 12: Comparison of peak SMD measured by SAMR and USAXS for conditions presented in Figure 45.

USAXS		120°			165°		
Radial Position (mm)	SMD (µm)	Radial Position (mm)	SMD (µm)	% Difference in SMD	Radial Position (mm)	SMD (µm)	% Difference in SMD
-0.077	30.8	0.0014	30.5	1%	.09	27.6	11%

Table 13: Comparison of USAXS and SAMR SMDs measured in the periphery of Spray D at an axial location of 10-mm. $\rho_{amb} = 1.2$ kg/m^3, $P_{inj} = 50$ MPa.

USAXS		90°		% Difference in SMD	% Difference in location
Radial Position (mm)	SMD (µm)	Radial Position (mm)	SMD (µm)		
0.11	16.2	0.13	15.2	6 %	16%
0.19	9.8	0.20	10.2	4%	11%
0.24	5.2	0.27	5.1	2%	9%

Figure 45 shows a comparison of the Phase III SAMR results (at 90°, 120°, 165° orientations) with USAXS results (at 0° orientation) for the condition Spray D 1.2 kg/m^3 50 MPa at 10-mm axial location. These results show good agreement despite the differing injector orientations. The 120° and 165° SAMR SMD results show good agreement with the USAXS results at the spray centerline as demonstrated in Table 12. The peak 120°-orientation SMD differs from the USAXS SMD by .98%, whereas the peak 165°-orientation SMD differs by 11.10%. The 90° orientation and the USAXS SMDs results converge at the spray periphery. Table 13 lists the periphery SMD data for the 90° orientation and the USAXS results. The minimal percent differences indicate the very good agreement between the two diagnostics. The SAMR diagnostic shows better agreement with the USAXS measurement for Phase III compared to Phase I.

5.2 Improved Spray Predictions with the KH-Faeth Spray Model

5.2.1 Conventional Spray Model Validation – Liquid and Vapor Penetration

Validation of the predicted liquid and vapor penetration rates is useful for assessing the accuracy of the modeled momentum transfer between the liquid phase and ambient gas phase. It is also the most commonly employed method for assessing spray model accuracy due to the abundance this type of experimental data. Evaluations of predicted spray penetration at non-vaporizing conditions and vaporizing condition have been conducted over various range of ECN injector setups as illustrated in Figure 46.

For the Spray A injector setup (Figure 46a), where relatively high temperature and high ambient density are characterized (vaporizing condition), the newly developed KH-Faeth model and the benchmark KH model predict a similarly accurate match to the experimental data. The similarity of the two models can lead to different conclusions. First, the details of the primary breakup model may not be heavily influential on the overall spray momentum exchange under such a highly evaporating condition. Second, it is also possible that the considered condition is not in favor of promoting turbulent-induced breakup; note that the ambient density is rather high, therefore the aerodynamic shear stress may be more predominant. In this case, the rate of emerging KH breakup regime out of KH-Faeth breakup competition may be outstanding; so it diminishes the effect of Faeth's turbulence breakup rate in the model.

A similar model validation and benchmarking was performed against data from a Spray D injector (Figure 46b). Again, both the benchmark KH model and the newly developed KH-Faeth model provide fairly good agreement with the experiments. One notably deviation from the experiments occurs under non-vaporizing conditions at high back-pressure (20 bar) and high ambient density (left side of Figure 46b), where the predicted liquid penetration rate lags the experiments for both models early in the injection process. There may be several possible reasons for this discrepancy during the transient period. One possibility is that the primary breakup physics are inaccurately represented in these models. To explore this idea, we performed

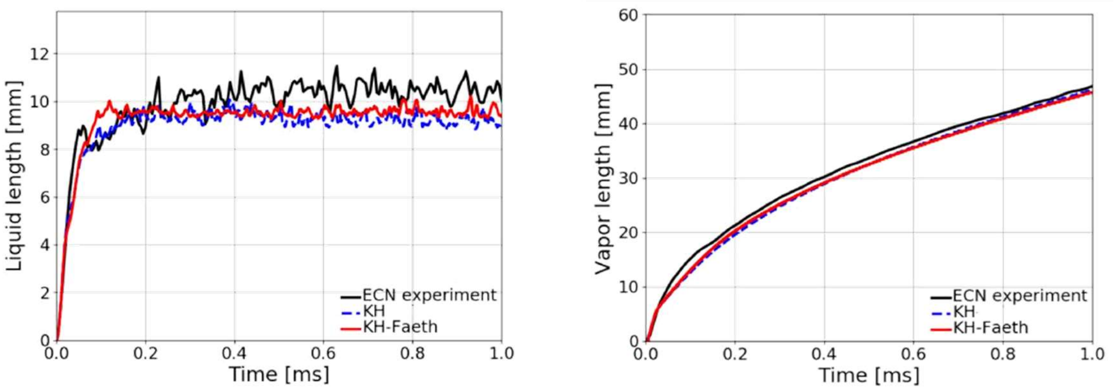

(a) Model predictions of Spray A liquid and vapor penetration using the newly developed KH-Faeth model and benchmark KH model. T_{amb} = 900 K, P_{amb} = 60 bar, ρ_{amb} = 22.8 kg/m3, P_{inj}=1500 bar.

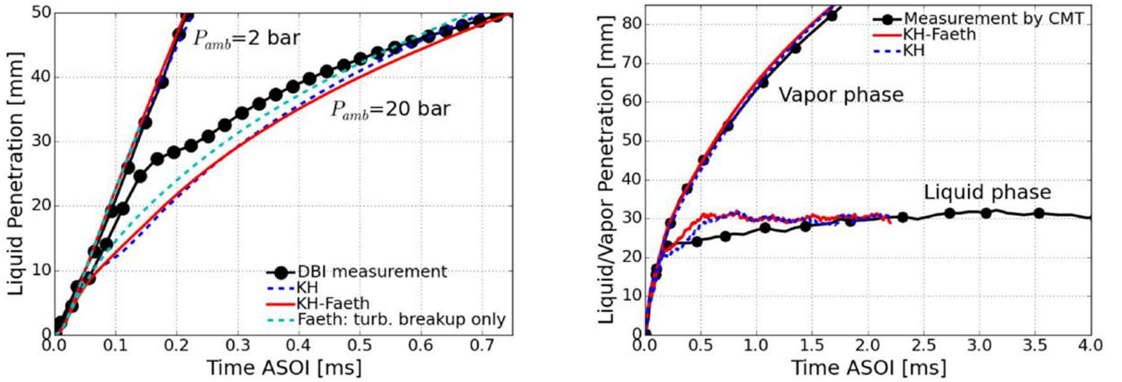

(b) Model predictions of Spray D liquid and vapor penetration using the newly developed KH-Faeth model and benchmark KH model. Left side: Non-vaporizing condition. T_{amb} = 303 K. Right side: Vaporizing condition. T_{amb} = 900 K, P_{amb} = 60 bar, ρ_{amb} = 22.8 kg/m3, P_{inj}=1500 bar.

Figure 46: Model evaluations of liquid and vapor penetration using ECN Spray A and Spray D injectors under non-vaporizing and vaporizing conditions. The experimental data for the Spray A injector setup was obtained from the ECN data library [92]. Spray D measurements under non-vaporizing conditions conducted at Georgia Tech as part of this project [147]. Vaporizing Spray D measurements from CMT-Motores Térmicos [148]

a simulation with the KH model deactivated in the KH-Faeth model setup, as shown as a cyan dashed line in the left side of Figure 46b, forcing the turbulent breakup model to act in isolation. This model prediction is found to be offset, somewhat closer to the measured liquid penetration curve, but still lacks the distinct two-phase transient behavior seen in the measurements. The good agreement found under quasi-steady injection conditions at later times suggests that errors are more likely due to inaccuracies in modeling the initial opening transient of the injector and effects on the nozzle flow and spray. Also, when using a Lagrangian-Eulerian spray modeling approach, such as that used here, liquid-gas momentum coupling in the near-nozzle regions may be especially prone to error since Lagrangian-Eulerian techniques are known to be highly grid dependent.

Ultimately, it is challenging to identify sources of model inaccuracy when validating spray models in this way. The liquid and vapor penetration measurements do not offer physical insight on the atomization process itself. Without this information, it is nearly impossible to formulate and accurate and predictable spray model for engine CFD codes. To address this knowledge gap, we developed an extensive body of SMD measurements for Spray A and Spray D as part of this project. In the following section of this report, we demonstrate a more quantitative validation of these models and demonstrate improved predictive and quantitative accuracy with the newly developed KH-Faeth model.

5.2.2 Advancement of Spray Model Validation via Detailed SMD Measurements

Validation of the models against USAXS measurements of SMD along the spray axis of ECN Spray D is shown in Figure 47 at a wide range of ambient conditions and injection pressures. Although the benchmark KH model and newly developed KH-Faeth models predicted similar spray penetration rates (Figure 46), the predicted axial SMD distributions can strongly differ, demonstrating significant variation in the predicted spray structure. In general, the newly developed KH-Faeth model is found to be more predictive across all test conditions, which includes a very wide span of ambient density condition. The benchmark KH model aligns well with the measured data at only a few conditions, with generally better performance at higher injection pressure (Figure 47d-f). These results suggest that the newly developed KH-Faeth model improves the predictive capabilities of spray models for diesel engine simulations, especially for low-load and early-injection types of conditions. Use of the benchmark KH model appears to be especially inappropriate at lower ambient density conditions, with the largest prediction errors at $P_{amb} = 1$ bar (Figure 47a andFigure 47d). This result is consistent with Wu and Faeth's experimental observations [23] that aerodynamic breakup is not predominate at high liquid-to-gas density ratios ($\rho_l / \rho_g > 500$).

To further assess the effect of ambient pressure on spray SMD and the suitability of breakup modeling approaches, a sensitivity analysis was conducted to compare the *response* of measured and predicted atomization characteristics to changes in ambient conditions. Figure 49 shows the relative change in SMD due to change in ambient gas density, indicated on the y-axis as SMD sensitivity to P_{amb}. Here, the sensitivity metric, $\bar{S}_{\hat{P}_{amb}}$, is defined as the fractional change of the location-specific averaged SMD value due to ambient pressure (or ambient density) change relative to standard atmospheric pressure ($P_{amb} = 1$ bar). For example, $\bar{S}_{\hat{P}_{amb}=2} = \overline{SMD}_{P_{amb}=2\ bar} \big/ \overline{SMD}_{P_{amb}=1\ bar}$, represents a relative change in ambient pressure

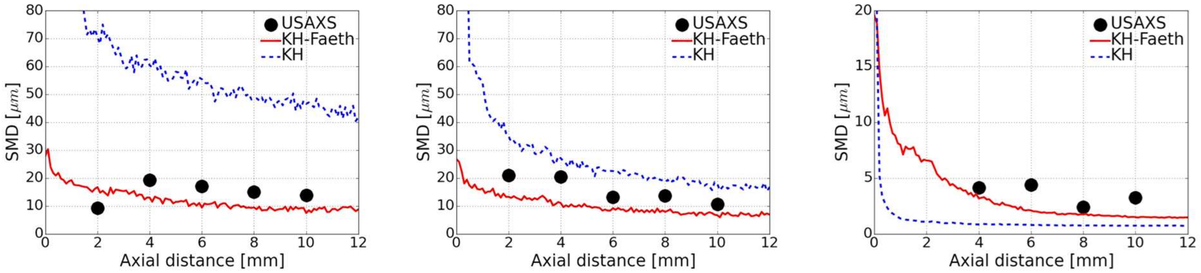

(a) P_{amb} = 1 bar, P_{inj} = 500 bar (b) P_{amb} = 2 bar, P_{inj} = 500 bar (c) P_{amb} = 20 bar, P_{inj} = 500 bar

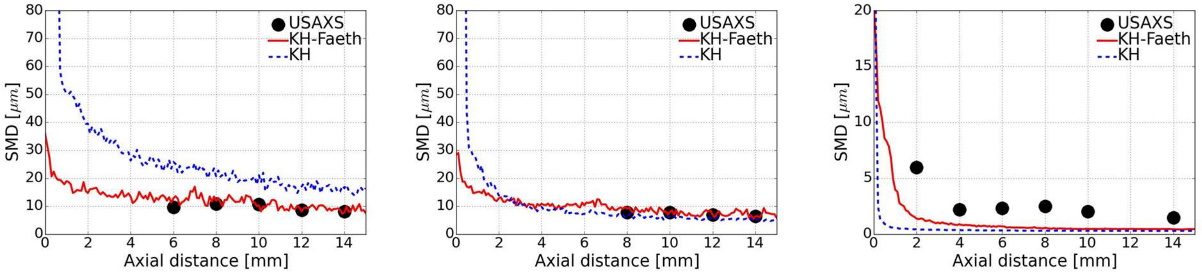

(d) P_{amb} = 1 bar, P_{inj} = 1500 bar (e) P_{amb} = 2 bar, P_{inj} = 1500 bar (f) P_{amb} = 20 bar, P_{inj} = 1500 bar

Figure 47: Comparison between predicted and measured (USAXS) SMD distributions along the spray centerline of ECN Spray D over a wide range of ambient conditions.

(or density) of 2x. The sensitivity parameters calculated and shown in Figure 49 are calculated from the average axial SMD at downstream locations of x = 8 mm and 10 mm.

As seen in Figure 49, the relative SMD change predicted by the newly developed KH-Faeth model tends to better follow the experimentally-measured SMD sensitivity at all conditions. However, a larger change in SMD is predicted at the highest ambient density and injection pressure condition. At this condition, aerodynamic shear stress on spray surface is high, and the aerodynamic KH breakup mechanism is expected to control the predicted droplet sizes. Indeed, both the benchmark KH and newly developed KH-Faeth models predict a similar SMD change at this condition, indicating that the KH model is dominant in the KH-Faeth model. The incorrect magnitude of the predicted SMD change relative to the experiments suggests that the KH model may fail to accurately represent aerodynamic breakup physics in real diesel sprays.

To further evaluate the physical predictions of the newly developed KH-Faeth model under the effect of ambient density, Figure 48 illustrates the likelihood of the model favoring turbulent breakup over aerodynamic breakup, based upon identification of the fastest breakup rate via Equation 9. The red contour represents regions with high dominance of turbulent breakup, while dark blue indicates dominance of aerodynamic breakup. As shown in Figure 48, regions of turbulent breakup are predicted throughout the entire spray plume at P_{amb} = 1 bar. whereas it only appears in the near-nozzle region at higher ambient density/pressure (P_{amb} = 20 bar) and vanishes rapidly downstream. Thus, even at high ambient density, droplet sizes are initially controlled by the turbulent breakup model, followed by a rapid transition to aerodynamic breakup. As seen previously in Figure 47c and Figure 47f, the KH-Faeth model also predicts an initial near-nozzle

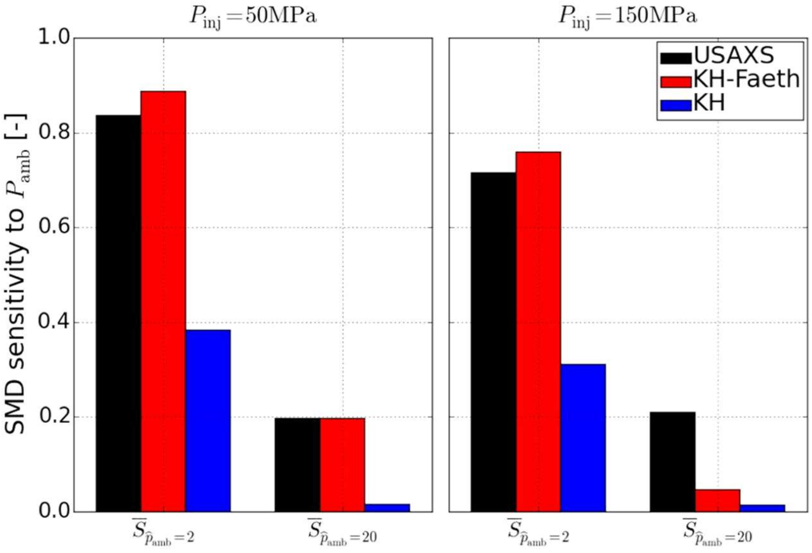

Figure 49: Sensitivity in the prediction and measurement of SMD due to a change in ambient pressure (density). ECN Spray D. Calculated from data shown in Figure 47.

SMD decay that better matches experimental measurements at the highest ambient density/pressure. This implies that even at high ambient densities, a turbulent breakup mechanism is still likely to be of relevance.

Although the benchmark KH and newly developed KH-Faeth models present noticeably different SMD distributions along the spray centerline at many conditions, the integrated liquid mass dispersion was found to be less deviated from each other. Figure 50 shows a comparison of the model-predicted and measured line-of-sight-integrated projected mass density in Spray D, as

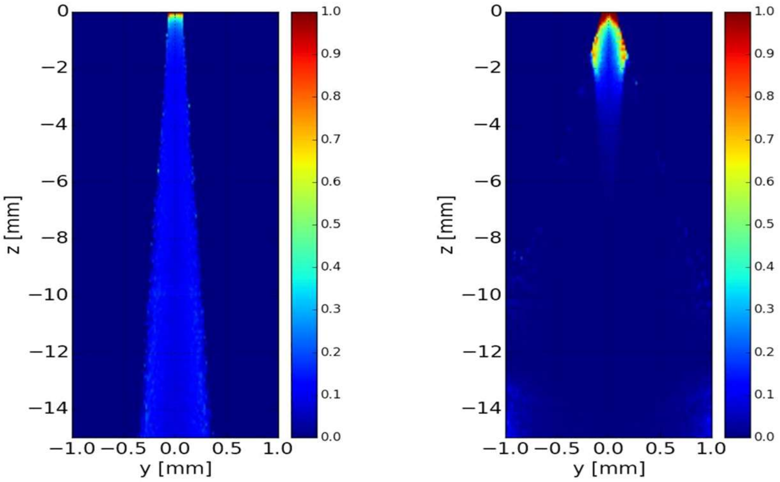

(a) P_{amb} = 1 bar

(b) P_{amb} = 20 bar

Figure 48: Probability of predicting turbulent breakup with newly developed KH-Faeth model under low (a) and high (b) ambient densities. Spray D. P_{inj} = 500 bar.

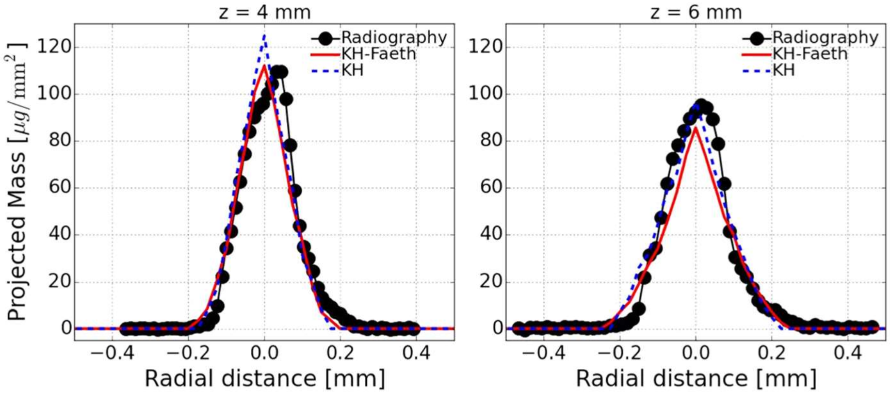

(a) P_{amb} = 1 bar, P_{inj} = 500 bar

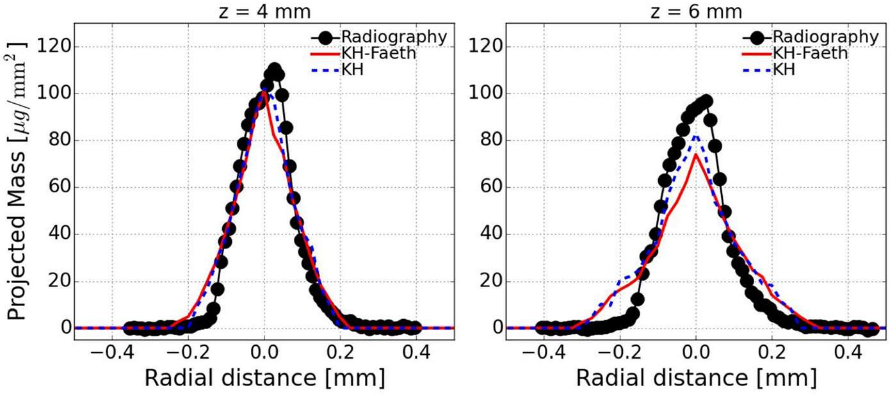

(b) P_{amb} = 2 bar, P_{inj} = 500 bar

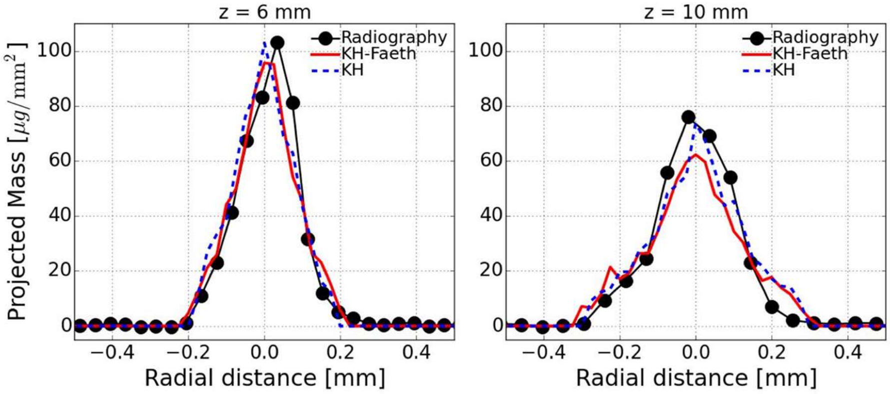

(c) P_{amb} = 1 bar, P_{inj} = 1500 bar

Figure 50: Comparison of predicted and measured line-of-sight-integrated liquid mass dispersion in Spray D at multiple downstream locations, as represented by the projected mass density (PMD).

measured from X-ray radiography experiments Argonne. These results demonstrate that measurements of projected density alone are insufficient for validation of breakup modeling approaches.

Figure 51 presents a comparison of the model predicted radial SMD distribution across Spray D compared against SAMR measurements taken during this project. In the preceding results, the benchmark KH and newly developed KH-Faeth models were employed without inclusion of a secondary breakup model. As shown in Figure 51a and Figure 51b, neglecting secondary breakup (solid lines) was found to lead to large errors in the predicted SMD at the spray periphery. Even though previous validation exercises showed good prediction accuracy along the spray centerline (Figure 47), significant deviation of the predicted SMD values occurs away from the spray axis. It is notable that this type of measurement is not readily available in the literature and offers a key enabling element to the validation of our newly developed spray model.

The prediction inaccuracies observed in Figure 51 motivated an evaluation of how the use of a secondary breakup model would impact the radial droplet size distribution. The resultant predicted SMDs with the commonly employed RT secondary breakup model are indicated by the dashed lines in Figure 51. Significant improvements in prediction accuracy are observed near the edges of the spray when the RT model is employed in conjunction with both the benchmark KH and newly developed KH-Faeth models, with only a small effect on the predicted centerline drop sizes. The impact of secondary RT breakup modeling on the predicted results is also seen to diminish with increasing ambient pressure (density).

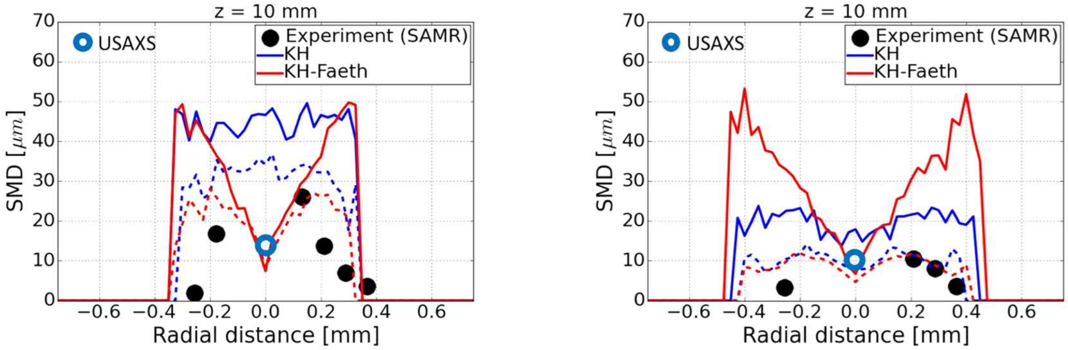

(a) P_{amb} = 1 bar (b) P_{amb} = 2 bar

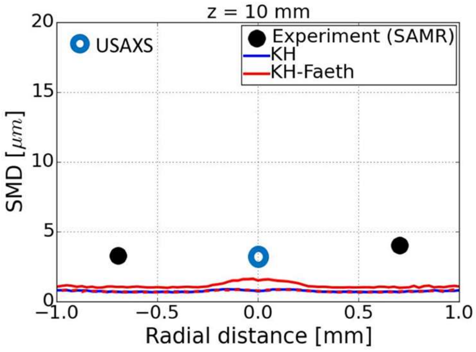

(c) P_{amb} = 20 bar

Figure 51: Simulated and measured SMD distribution in transverse direction: solid line and dashed line indicate the calculated SMD values with and without secondary breakup (RT model), respectively. Spray D, P_{inj} = 500 bar.

In summary, the newly-develop KH-Faeth spray model predicts global and local spray characteristic more accurately than the widely adopted and employed KH model. In particular, predicted drop size distributions are seen to predict measured SMDs both *quantitatively* and *predictively*, with accurate response in droplet size distributions over a wide range of ambient density, injection pressure, and injector nozzle size (Spray A and D).

6 Products

1. S. Kim, “Advancing Turbulent Spray and Combustion Models for Compression Ignition Engine Simulations,” Ph.D. Thesis, Georgia Institute of Technology, 2019.
2. Martinez, G. L., Poursadegh, F., Magnotti, G. M., Matusik, K. E., Duke, D. J., Knox, B. W., … Genzale, C. L. (2019). Measurement of Sauter mean diameter in diesel sprays using a scattering–absorption measurement ratio technique. *International Journal of Engine Research*, *20*(1), 6–17.
3. K. E. Matusik, B. A. Sforzo, H. J. Seong, D. J. Duke, A. L. Kastengren, J. Ilavsky, & C. F. Powell (2019). X-Ray Measurements of Fuel Spray Specific Surface Area and Sauter Mean Diameter for Cavitating and Non-Cavitating Diesel Sprays. *Atomization and Sprays,* 29(3), 199-216.
4. G.L. Martinez, “Extinction Droplet Sizing Measurements in Diesel-Relevant Sprays,” M.S. Thesis, Georgia Institute of Technology, 2018.
5. G.L. Martinez, F. Poursadegh, G. M. Magnotti, K. E. Matusik, D. J. Duke, B. W. Knox, C. L. Genzale, C. F. Powell, and A. L. Kastengren, “Measurement of Sauter Mean Diameter (SMD) in Diesel Sprays Us-ing a Scattering-Absorption Measurement Ratio Technique,” Conference on Thermo- and Fluid Dynamic Processes in Direct Injection Engines (THIESEL 2018). September 2018.
6. S. Kim, G. L. Martinez, B. F. Yraguen, G. M. Magnotti, K. E. Matusik, B. A. Sforzo, A. L. Kastengren, C. F. Powell, T. Lucchini, G. D’Errico, B. W. Knox, C. L. Genzale, “Validation of a New Turbulence-Induced Lagrangian Primary Breakup Model for Diesel Spray Atomization,” International Conference on Liquid Atomization and Spray Systems (ICLASS). July 2018.
7. Magnotti, G.M. and Genzale, C.L., “Exploration of turbulent atomization mechanisms for diesel spray simulations,” SAE Technical Paper 2017-01-0829, 2017.
8. Magnotti, G.M., Matusik, K.E., Duke, D.J., Knox, B.W., Martinez, G.L., Powell, C.F., Kastengren, A.L. and Genzale, C.L., “Modeling the influence of nozzle-generated turbulence on diesel sprays,” 29th Annual Conference of the Institute for Liquid Atomization and Spraying Systems (ILASS)-Americas Conference, Atlanta, GA, May 2017.
9. Martinez, G.L., Magnotti, G.M., Knox, B.W., Matusik, K.E., Duke, D.J., Kastengren, A.L., Powell, C.F. and Genzale, C.L., “Quantification of sauter mean diameter in diesel sprays using scattering-absorption extinction measurements,” 29th Annual Conference of the Institute for Liquid Atomization and Spraying Systems (ILASS)-Americas Conference, Atlanta, GA, May 2017.
10. G.M. Magnotti, “Modeling the Influence of Nozzle-Generated Turbulence on Diesel Sprays,” Ph.D. Thesis, Georgia Institute of Technology, 2017.

7 References

1. F. R. Westlye, K. Penney, A. Ivarsson, L. Pickett, J. Manin and S. Skeen, "Diffuse back-illumination setup for high temporally resolved extinction imaging," Applied Optics, 2017.

2. Y. Yue, C. F. Powell, R. Poola, J. Wang and J. K. Schaller, "Quantitative measurements of diesel fuel spray characteristics in the near-nozzle region using x-ray absorption," Atomization and Sprays, vol. 11, pp. 471-490, 2001.

3. J. Wang, "X-ray vision of fuel sprays," Journal of Synchotron Radiation, vol. 12, pp. 197-207, 2005.

4. G. L. Martinez, F. Poursadegh, G. M. Magnotti, B. W. Knox, C. L. Genzale, K. E. Matusik, D. J. Duke, C. F. Powell and A. L. Kastengren, "Measurement of Sauter mean diameter (SMD) in Diesel sprays using a scattering-absorption measurement (SAMR) technique," in Thermo and Fluid Dynamics Processes in Direct Injection Engines, Valencia, 2018.

5. A. L. Kastengren, C. F. Powell, D. Arms, E. M. Dufresne, H. Gibson and J. Wang, "The 7BM beamline at the APS: a facility for time-resolved fluid dynamics measurements," Journal of Synchrotron Radiation, vol. 19, pp. 654-657, 2012.

6. G. L. Martinez, G. M. Magnotti, B. W. Knox, K. E. Matusik, D. J. Daniel, C. L. Genzale, C. F. Powell and A. L. Kastengren, "Quantification of Sauter mean diameter in diesel sprays using scattering-absorption extinction measurements," in Institute for Liquid Atomization and Spray Systems, Atlanta, 2017.

7. K. E. Matusik, B. A. Sforzo, H. J. Seong, D. J. Duke, A. L. Kastengren, J. Ilavsky and C. F. Powell, "X-Ray Measurements of Fuel Spray Specific Surface Area and Sauter Mean Diameter," in International Conference on Liquid Atomization and Spray Systems, Chicago, 2018.

8. Glatter, O., and Kratky, O., “Small-angle X-ray Scattering,” Academic Press, London, 1982.

9. van de Hulst, H.C., “Light Scattering by Small Particles,” (New York, Dover Publications, 1981).

10. MiePlot, http://www.philiplaven.com/mieplot.htm, Retrieved Feb. 2016.

11. A. Kastengren, J. Ilavskya, J. P. Vierab, R. Payri, D. Duke, A. Swantek, F. Z. Tiloccoc, N. Sovis, and C. Powell, “Measurements of droplet size in shear-driven atomization using ultra small angle x-ray scattering,” International Journal of Multiphase Flows, 2017.

12. C. Powell, D. Duke, A. Kastengren, and J. Ilavsky, “Measurements of diesel spray droplet size with ultra-small angle x-ray scattering,” in 25th ILASS Americas conference, Pittsburgh, PA, 2013.

13. A. L. Kastengren, C. F. Wang, K. S. Im and J. Wang, "X-ray radiography measurements of diesel spray structure at engine-like ambient density," Atomization and Sprays, vol. 19, no. 11, 2009.

14. E. Berrocal, "Multiple scattering of light in optical diagnostics of dense sprays and other complex turbid media," Cranfield University, 2006.

15. E. Berrocal, D. L. Sedarsky, M. E. Paciaroni, I. V. Meglinski and M. A. Linne, "Laser light scattering in turbid media part 1: experimental and simulated results for the spatial intensity distribution," Optics Express, vol. 15, pp. 10649-10665, 2007.

16. G. M. Magnotti, K. E. Matusik, D. J. Duke, B. W. Knox, G. L. Martinez, C. F. Powell, A. L. Kastengren and C. L. Genzale, "Modeling the Influence of Nozzle-Generated Turbulence on Diesel Sprays," in ILASS-Americas 29th Annual Conference on Liquid Atomization and Spray Systems, Atlanta, 2017.

17. J. Labs and T. Parker, "Diesel fuel spray droplet sizes and volume fractions from the region 25mm below the orifice," Atomization and Sprays, vol. 13, pp. 45-62, 2003.

18. R. Payri, L. Araneo, J. Shakal and V. Soare, "Phase doppler measurements: system set-up optimization for characterization of a diesel nozzle," Journal of mechanical science and technology, vol. 22, no. 8, pp. 1620-1632, 2008.

19. G. J. Smallwood and O. L. Gulder, "Views on the structure of transient diesel sprays," Atomization and Sprays, vol. 10, pp. 355-386, 2000.

20. K. J. Wu, R. D. Reitz and F. V. Bracco, "Measurements of drop size at the spray edge near the nozzle in atomizing liquid jets," Physics of Fluids, vol. 4, no. 29, pp. 941-951, 1986.

21. H. Kosaka, T. Suzuki and T. Kamimoto, "Numerical simulation of turbulent dispersion of fuel droplets in an unsteady spray via discrete vortex method," SAE Technical Paper, 1995.

22. J. Labs and T. Parker, "Two-dimensional droplet size and volume fraction distributions from the near-injector region of high-pressure diesel sprays," *Atomization and Sprays,* vol. 16, pp. 843-855, 2006.

23. P.-K. Wu and G. Faeth, “Aerodynamic effects of primary breakup of turbulent liquids,” Atomization and Sprays, vol. 3, no. 3, pp. 265–289, 1993.

24. K. DeJuhasz, “Dispersion of sprays in solid injection oil engines,” Transactions of American Society of Mechanical Engineers, vol. 53, 1931.

25. P. Schweitzer, “Mechanism of disintegration of liquid jets,” Journal of Applied Physics, vol. 8, 1937.

26. G. Sitkei, “On the theory of jet atomization,” Acta Tech. Acad. Sci. Hungaricae, vol. 25, 1959.

27. G. Faeth, L.-P. Hsiang, and P.-K. Wu, “Structure and breakup properties of sprays,” International Journal of Multiphase Flow, vol. 21, pp. 99–127, 1995.

28. D. Lee and R. Spencer, “Photomicrographic studies of fuel sprays,” N.A.C.A. Report No. 454, 1933.

29. P.-K. Wu, L.-K. Tseng, and G. Faeth, “Primary breakup in gas/liquid mixing layers for turbulent liquids,” Atomization and Sprays, vol. 2, pp. 295–317, 1992.

30. P.-K. Wu, R. Mirand, and G. Faeth, “Effects of initial flow conditions on primary breakup of nonturbulent and turbulent round liquid jets,” Atomization and Sprays, vol. 5, pp. 175–196, 1995.

31. B. Munson, T. Okiishi, W. Huebsch, and A. Rothmayer, Fundamentals of Fluid Mechanics. Hoboken, NJ: John Wiley & Sons, 2013.

32. A. L. Kastengren, F. Z. Tilocco, C. F. Powell, J. Manin, L. M. Pickett, R. Payri, and T. Bazyn, “Engine combustion network (ECN): Measurements of nozzle geometry and hydraulic behavior,” Atomization and Sprays, vol. 22, no. 12, pp. 1011–1052, 2012.

33. C. Dumouchel, “On the experimental investigation on primary atomization of liquid streams,” Experiments in Fluids, vol. 45, pp. 371–422, Jun 2008.

34. T. Karasawa, M. Tanaka, K. Abe, S. Shiga, and T. Kuruabayashi, “Effect of nozzle configuration on the atomization of a steady spray,” Atomization and Sprays, vol. 2, pp. 411–426, 1992.

35. N. Tamaki, M. Shimizu, K. Nishida, and H. Hiroyasu, “Effects of cavitation and internal flow on atomization of a liquid jet,” Atomization and Sprays, vol. 8, pp. 179–197, 1998.

36. R. D. Reitz, “Modeling atomization processes in high-pressure vaporizing sprays,” Atomization and Sprays, vol. 3, pp. 309–337, 1987.

37. S. Som, Development and Validation of Spray Models for Investigating Diesel Engine Combustion and Emissions. PhD thesis, University of Illinois at Chicago, 2009.

38. J. C. Beale and R. D. Reitz, “Modeling spray atomization with the Kelvin-Helmholtz/Rayleigh-Taylor hybrid model,” Atomization and Sprays, vol. 9, pp. 623–650,1999.

39. G.M. Magnotti, “Modeling the Influence of Nozzle-Generated Turbulence on Diesel Sprays,” Ph.D. Thesis, Georgia Institute of Technology, 2017.

40. C.-M. Termicos, “Engine combustion network experimental data archive.” https://www.cmt.upv.es/ECN03.aspx#model.

41. Engine Combustion Network (ECN), “Engine combustion network experimental data archive.” http://www.sandia.gov/ECN.

42. Knox, B.W., Genzale, C.L., "Effects of End-of-Injection Transients on Combustion Recession in Diesel Sprays," SAE Int. J. Engines, 9(2), 2016.